IEEE Access
Multidisciplinary ⋮ Rapid Review ⋮ Open Access Journal

Received 14 August 2022, accepted 25 September 2022, date of publication 28 September 2022,
date of current version 10 October 2022.

Digital Object Identifier 10.1109/ACCESS.2022.3210550

RESEARCH ARTICLE

Disturbance Observer-Based Force Estimation and Fault Detection for Robotic Manipulator in Radioactive Environments

HUAIMIN LIU[1], XIANGJIANG WANG[1], AND LIUYANG CHEN[2]
[1]College of Resource Environmental and Safety Engineering, University of South China, Hengyang 421001, China
[2]Department of Mechanical Engineering, University of South China, Hengyang 421001, China

Corresponding author: Xiangjiang Wang (wangxiangjiang72@163.com)

This work was supported by the Local Scientific and Technological Development of China's Central Government under Grant 2022ZYQ015.

ABSTRACT Robotic systems with force sensing have great potential for use in radioactive environments. In this study, a modified observer-based method was developed to calculate the unknown external force without adding a redundant sensor and achieve the fault detection in the presence of a force sensor. A dynamic model of a serial robotic manipulator was built and the design procedure for a modified disturbance observer (MDO) was established. The output of observer was then used to suppress the disturbance and generate the fault signature. Moreover, the stability analysis shows that the convergence of the observer error is ultimately bounded. Simulation results under the step and composite sinusoidal disturbance torque demonstrate the performance of the force estimation and disturbance rejection. The results, obtained using the Kinova Jaco^2 robot manipulator, show that the estimated errors of the external force in X-Y-Z direction are bounded within ± 0.5 N, ± 2 N, and ± 3 N, respectively. Finally, the effectiveness of fault detection is also verified by the experiment results.

INDEX TERMS Robotic manipulator, observer-based, force estimation, fault detection.

I. INTRODUCTION

Over the past several decades, nuclear energy has been applied extensively in civilian domains, such as nuclear power plant, nuclear medicine, and food-processing. It is highly convenient for mankind, but also has negative effects to human environmental health. Radioactive waste is one of the major hazards of the environment and human health. This type of hazardous waste exits harmful radiations and may lead the human operators to infections and diseases. Therefore, the nuclear industry worldwide has been seeking the cost-effective approaches for the safe disposal of radioactive waste [1]. The use of robotics and remote technologies provides a safe approach to complete a lot of dangerous tasks which the human beings had to perform earlier. These tasks often involve robot-environment interactions, such as dismantling and packing the reactor vessel internals and grasping the pieces of nuclear fuel bundle. Force interactions with surrounding objects are essential for guaranteeing safe task performance. Hence, there is a need to implement the force control for the robotic manipulators to achieve compliant and safe movement, which requires the information of robot-environment interaction forces [2]. The typical method for acquiring the information of interaction force is to equip the force/torque sensors of the high-resolution and reliability on the wrist of robot manipulator. However, these sensors result in a significant increase in the cost of the robotic system and the complexity of the software and hardware design. Moreover, the performance of these sensors is easy to be affected by the radioactive environment (high temperature, high doses of radiation and strong disturbance) [3]. On the other hand, with the growing requirements on the safety and reliability of robotic system in radioactive environments, fault diagnosis via hardware redundancy may not be an appropriate option for robotic systems due to the radiation damage of the hardware. Therefore, the more effective strategies

The associate editor coordinating the review of this manuscript and approving it for publication was Baoping Cai.

of fault detection without additional hardware need to be addressed.

To overcome the above mentioned drawbacks of the deployment of force sensors, force estimation methods provide a means of quantifying the forces and torques exerted into a robotic system, which is an alternative solution to eliminate the need for expensive force sensors in strong radiation environments. Several studies have been conducted in the field of robotics to estimate the interaction force without using force sensors. The most direct estimation method is to use the available measurements, such as the motor torque, joint position, velocity, and acceleration to estimate the external force [4], [5]. However, the acceleration signal is not available or is difficult to obtain from the joint position signal owing to the noise sensitivity of the second order differential, so this method is not practical to implement. An external force estimation using a comprehensive dynamic model was developed, where the model was divided into the dynamic and quasi-static modes [6]. Nevertheless, this model-based estimation is limited by the parameter uncertainty and unmodelled nonlinear effects and the precision of force estimation is not guaranteed. To avoid the calculation of the joint acceleration, generalized momentum-based methods to calculate the interaction force were adopted by [7]. This generalized momentum-based method can guarantee that the estimated torques quickly converge to the actual ones, but the inertia parameters are required in the generalized momentum. A robust force estimation scheme based on a semi-parametric model and a disturbance Kalman filter (DKF) was introduced to detect the interaction force for a multi-link manipulator [8]. This scheme considers the manipulator's model as well as the disturbance model, which improves the robustness against uncertainty. However, the performance of this scheme can be worsened by the neglected dynamic uncertainty. In addition, an extended state observer (ESO) was developed for estimating the time-varying external forces on a robotic manipulator [9]. Nevertheless, the model errors of the robot dynamic model reduce the accuracy of the ESO observer, and the high frequency tremors may limit the suitability of the method. A second-order sliding-mode observer was designed for estimating the interacting force on a robot manipulator [10]. This observer can calculate the external force exerted by the environment without disturbance, which restricts the application of the observer, particularly in realistic robotic systems.

Recently, a higher-order sliding mode observer was developed for the online monitoring of unknown external force/torque. This method regards the torque disturbance as an unknown input and reconstructs the torque disturbance by using robust sliding mode (SM) terms [11]. An interaction force estimation method based on a higher-order sliding mode observer (HOFTO) was introduced to evaluate the fast-varying external forces acting on the ER3A robot. The HOFTO can achieve a higher estimation accuracy and better system performance than the traditional ESO method. However, this method is still sensitive to unmodelled effects and sensor noise, which results in estimation errors [12]. Another force estimation method was the use of the disturbance observers (DOB), which reconstructs the unknown the external force on the robotic manipulation from the known inputs and the measurable output [13]. The estimation accuracy of the DOB is theoretically guaranteed because the estimation of the system state converges to the vicinity of the actual states [14]. Furthermore, the non-linear disturbance observer (NDOB) was extended to nonlinear and coupled systems for the estimation of robot-environment interaction [15], [16], [17].

On the other hand, various advanced control techniques have been proposed to estimate the unmodeled dynamics and suppress the disturbances, such as sliding mode control (SMC) [18], [19], robust control [20], [21], adaptive control [22], [23], neural network control [24], [25], [26]. For example, the adaptive control or robust control was applied to the controller that handle unforeseen influences to a limited extent [27]. The neural network control was used to compensate the influence of unknown dynamics and uncertainties [28], [29]. However, among the various methods of disturbance rejection, disturbance observer-based control scheme is the most efficient way to handle the disturbance effect. The basic concept behind disturbance observer-based control is to lump all the system uncertainties into the disturbance term and to estimate the lumped term. Then, the effect of the disturbance can be cancelled out by introducing feedforward compensation. For the fault diagnosis of the robot system, several types of observer-based fault diagnosis approaches have been developed. An optimal placement of sensors based on a discrete particle swarm algorithm was developed for the fault diagnosis of hydraulic control system [30]. A high-gain observer was designed for fault diagnosis of the ANAT robot [31]. A proportional integral observer-based fault detection was proposed on the basis of the robust adaptive fuzzy sliding mode extended autoregressive exogenous input–Laguerre model for a robot manipulator [32]. A data-driven method-based fault diagnosis approach based on the deep convolutional neural network is used to recognize the sensor and actuator faults of the robot system [33]. a fault diagnosis scheme based on the adaptive observer is proposed for the actuator fault in the networked manipulator system, which the residual of the time-delay state is used to design the fault estimation law [34].

Motivated by the above-mentioned works, we presented a novel method to calculate the external forces and detect the sensor faults. The main contributions of this study can be summarized as follows: a) A modified disturbance observer-based method is proposed for calculating the unknown external force without additional hardware and detecting the sensor fault in the presence of a force sensor, which can enhance the safety and reliability of the robotic system in radioactive environments. b) A Lyapunov stability analysis is considered to illustrate the stability of the modified disturbance observer and the observer error asymptotically converge to be ultimately bounded. c) Simulations and experiments performed on the Kinova Jaco^2 manipulator verified

the performance of the observer-based force estimation and fault detection.

The remainder of this article is organized as follows. The dynamic model and properties of a serial multiple-joint manipulator are presented in Section 2. The modified disturbance observer design, stability analysis, and fault detection are detailed in Section 3. Simulation studies for different scenarios are given in Section 4. Experiments are performed in Section 5 to illustrate the effectiveness of the proposed force estimation and fault detection method. Finally, Section 6 outlines the conclusions.

II. ROBOT DYNAMIC MODEL AND PROPERTIES

According to the recursive Newton-Euler method [35], the dynamic equations of n joint manipulator systems can be described as:

$$\boldsymbol{D}(\boldsymbol{q})\ddot{\boldsymbol{q}} + \boldsymbol{C}(\boldsymbol{q}, \dot{\boldsymbol{q}}) + \boldsymbol{G}(\boldsymbol{q}) + \boldsymbol{F}(\dot{\boldsymbol{q}}) = \boldsymbol{\tau} + \boldsymbol{\tau}_{ext} \tag{1}$$

where $\boldsymbol{D}(\boldsymbol{q}) \in \boldsymbol{R}^{n\times n}$ refers to the symmetric inertial matrix, $\boldsymbol{C}(\boldsymbol{q}, \dot{\boldsymbol{q}}) \in \boldsymbol{R}^{n\times n}$ denotes the nonlinear Coriolis and centrifugal torque vector and $\boldsymbol{G}(\boldsymbol{q}) \in \boldsymbol{R}^n$ denotes the gravity loading force vector and $\boldsymbol{F}(\dot{\boldsymbol{q}}) \in \boldsymbol{R}^n$ denotes the friction torque vector; $\boldsymbol{q}, \dot{\boldsymbol{q}}, \ddot{\boldsymbol{q}} \in \boldsymbol{R}^n$ refer to the joint position vector, velocity vector and joint acceleration vector, respectively; $\boldsymbol{\tau} \in \boldsymbol{R}^n$is the actuator torque acting on the joints. $\boldsymbol{\tau}_{ext} \in \boldsymbol{R}^n$ denotes an unknown external joint torque vector.

Although several types of effective friction models have been proposed for the mechanical systems, the classical Coulomb-viscous friction model is still widely used to model joint friction in robotic applications [36]. The friction torque model is given by:

$$\boldsymbol{F}(\dot{\boldsymbol{q}}) = \boldsymbol{f}_c sign(\dot{\boldsymbol{q}}) + \boldsymbol{f}_v\dot{\boldsymbol{q}} = [sign(\dot{\boldsymbol{q}}), \dot{\boldsymbol{q}}] \cdot [\boldsymbol{f}_c, \boldsymbol{f}_v] \tag{2}$$

where $\boldsymbol{f}_c \in \boldsymbol{R}^n$ denotes the Coulomb coefficients vector; $\boldsymbol{f}_v \in \boldsymbol{R}^n$ denotes viscous friction coefficients vector. $sign(\cdot)$ represents a sign function.

The important properties of the dynamic model (1) utilized in convergence analysis and control system design are given as follows:

Property 1: The matrix $\dot{\boldsymbol{D}}(\boldsymbol{q}) - 2\boldsymbol{C}(\boldsymbol{q}, \dot{\boldsymbol{q}})$ is a skew-symmetric matrix, and it can be derived as $\dot{\boldsymbol{D}}(\boldsymbol{q}) = \boldsymbol{C}(\boldsymbol{q}, \dot{\boldsymbol{q}}) + \boldsymbol{C}(\boldsymbol{q}, \dot{\boldsymbol{q}})^T$.

Property 2: The inertia matrix $\boldsymbol{D}(\boldsymbol{q})$ is symmetric, positive-definite and bounded by the positive constants d_1 and d_2. The following inequality holds:

$$d_1 \|\boldsymbol{x}\|^2 \le \boldsymbol{x}^T\boldsymbol{D}(\boldsymbol{q})\boldsymbol{x} \le d_2 \|\boldsymbol{x}\|^2 \tag{3}$$

where $\boldsymbol{x}$ is an identity matrix.

Property 3: $\boldsymbol{C}(\boldsymbol{q}, \dot{\boldsymbol{q}})$ and $\boldsymbol{G}(\boldsymbol{q})$ are upper bounded by known bounds as follows:

$$\|\boldsymbol{C}(\boldsymbol{q}, \dot{\boldsymbol{q}})\|^2 \le k_c \|\dot{\boldsymbol{q}}\|, \quad \|\boldsymbol{G}(\boldsymbol{q})\| \le k_g \tag{4}$$

where k_c and k_g are bounded positive constant.

Assumption 1: The actuator torque $\boldsymbol{\tau}$ and its time derivative are upper bounded.

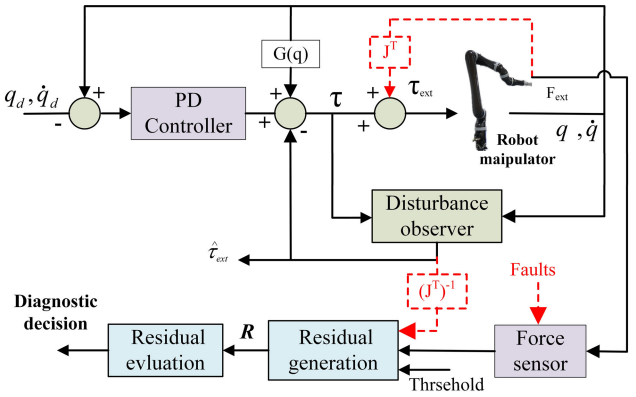

FIGURE 1. Control strategy for robot manipulator.

Assumption 2: External joint torque $\boldsymbol{\tau}_{ext}$ and its time derivative are bounded by known limits.

The motion control objective is to make the actual joint position $\boldsymbol{q}$ converge to a given desired joint position $\boldsymbol{q}_d$. the error vector of the position and velocity can be obtained as:

$$\boldsymbol{e}(t) = \boldsymbol{q}_d(t) - \boldsymbol{q}(t), \quad \dot{\boldsymbol{e}}(t) = \dot{\boldsymbol{q}}_d(t) - \dot{\boldsymbol{q}}(t) \tag{5}$$

To achieve the purpose of control, the position error vector $\boldsymbol{e}(t)$ and velocity error vector $\dot{\boldsymbol{e}}(t)$ vanishes asymptotically.

$$\lim_{t\to\infty} \boldsymbol{e}_{(t)} = 0, \quad \lim_{t\to\infty} \dot{\boldsymbol{e}}(t) = 0 \tag{6}$$

The composite controller consists of a linear proportional derivative (PD) controller and a disturbance observer. The undesirable effects of external force/torque and other disturbances are compensated by the outputs of the disturbance observer through feedforward technology, which enhances the disturbance attenuation ability for the composite controller. Thus, the control law can be written as:

$$\boldsymbol{\tau} = \boldsymbol{G}(\boldsymbol{q}) + \boldsymbol{K}_p\boldsymbol{e}(t) + \boldsymbol{K}_d\dot{\boldsymbol{e}}(t) - \hat{\boldsymbol{\tau}}_{ext} \tag{7}$$

where $\boldsymbol{K}_p$ and $\boldsymbol{K}_d$ are symmetric, positive-definite matrix with constant value and act as the proportional and derivative gains, respectively. $\boldsymbol{G}(\boldsymbol{q})$ is the online gravity compensation. $\hat{\boldsymbol{\tau}}_{ext}$ is the estimate vector of external joint torque. The control strategy of observer-based force estimation and fault detection is shown in Fig. 1.

III. OBSERVER DESIGN AND STABILITY ANALYSIS

A disturbance observer (DOB) was originally proposed in [37] for the robotic application as an unknown input observer. The core concept of this type observer is to utilize the known control inputs and the measured outputs to reconstruct unknown disturbances. With the measurable joint acceleration information and considering the external force as the disturbance, the following disturbance observer was developed for the model (1) [38]:

$$\dot{\hat{\boldsymbol{\tau}}}_{ext} = -\boldsymbol{L}\hat{\boldsymbol{\tau}}_{ext} + (\boldsymbol{D}(\boldsymbol{q})\ddot{\boldsymbol{q}} + \boldsymbol{C}(\boldsymbol{q}, \dot{\boldsymbol{q}}) + \boldsymbol{F}(\dot{\boldsymbol{q}}) - \boldsymbol{\tau}) \tag{8}$$

where $\boldsymbol{L}$ denotes the diagonal gain matrix. Defining $\boldsymbol{s} = \boldsymbol{\tau}_{ext} - \hat{\boldsymbol{\tau}}_{ext}$ as the observer error, the dynamics of the observer

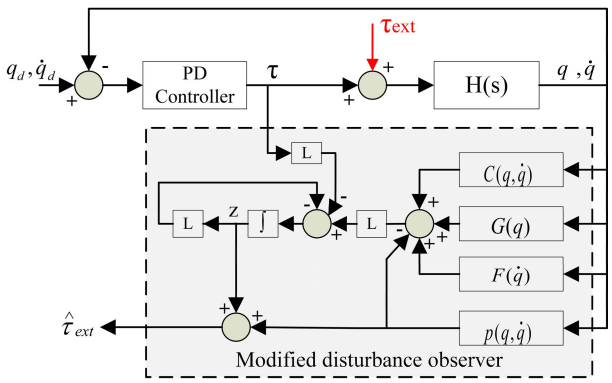

FIGURE 2. Structure of modified disturbance observer for external torque estimation.

error can be obtained from (1) and (8).

$$\boldsymbol{s} = \dot{\boldsymbol{\tau}}_{ext} - \boldsymbol{L}\boldsymbol{s} \tag{9}$$

The dynamics of observer error (9) is asymptotically stable by the proper choice of gain matrix $\boldsymbol{L}$ when the external joint torque tends to be constant. As seen in (8), the joint acceleration measurement $\ddot{\boldsymbol{q}}$ is required for the implementation of the disturbance observer. However, the joint acceleration measurement cannot be obtained from the joint position or velocity measurement by differentiation owing to measurement noise. Installing an accurate accelerometer for acceleration measurement is impractical in robotic manipulators due to its difficult integration and the reliability.

To overcome the limitation of the observer (8), a new auxiliary variable $\boldsymbol{z}$ is introduced to remove the dependence of the acceleration measurement.

$$\boldsymbol{z} = \hat{\boldsymbol{\tau}}_{ext} + \boldsymbol{p}(\boldsymbol{q}, \dot{\boldsymbol{q}}) \tag{10}$$

where $\boldsymbol{z} \in \boldsymbol{R}^n$ donates the auxiliary state variable vector, $\boldsymbol{p}(\boldsymbol{q}, \dot{\boldsymbol{q}}) \in \boldsymbol{R}^n$ donate the auxiliary function to be designed. It is assumed that the following nonlinear equation is satisfied:

$$\boldsymbol{L}\boldsymbol{D}(\boldsymbol{q})\ddot{\boldsymbol{q}} = \begin{bmatrix} \dfrac{\partial \boldsymbol{p}(\boldsymbol{q}, \dot{\boldsymbol{q}})}{\partial \boldsymbol{q}} & \dfrac{\partial p(\boldsymbol{q}, \dot{\boldsymbol{q}})}{\partial \dot{\boldsymbol{q}}} \end{bmatrix} \begin{bmatrix} \boldsymbol{q} \\ \ddot{\boldsymbol{q}} \end{bmatrix} = \dot{\boldsymbol{p}}(\boldsymbol{q}, \dot{\boldsymbol{q}}) \tag{11}$$

Considering (10), (11) and (8), implies that

$$\begin{aligned} \dot{\boldsymbol{z}} &= \dot{\hat{\boldsymbol{\tau}}}_{ext} - \dot{\boldsymbol{p}}(\boldsymbol{q}, \dot{\boldsymbol{q}}) \\ &= -\boldsymbol{L}\hat{\boldsymbol{\tau}}_{ext} + \boldsymbol{L}(\boldsymbol{D}(\boldsymbol{q})\ddot{\boldsymbol{q}} + \boldsymbol{C}(\boldsymbol{q}, \dot{\boldsymbol{q}}) + \boldsymbol{G}(\boldsymbol{q}) + \boldsymbol{F}(\dot{\boldsymbol{q}}) - \boldsymbol{\tau}) - \dot{\boldsymbol{p}}(\boldsymbol{q}, \dot{\boldsymbol{q}}) \\ &= -\boldsymbol{L}\hat{\boldsymbol{\tau}}_{ext} + \boldsymbol{L}(\boldsymbol{C}(\boldsymbol{q}, \dot{\boldsymbol{q}}) + \boldsymbol{G}(\boldsymbol{q}) + \boldsymbol{F}(\dot{\boldsymbol{q}}) - \boldsymbol{\tau}) \\ &\quad + \underbrace{\boldsymbol{L}\boldsymbol{D}(\boldsymbol{q})\ddot{\boldsymbol{q}} - \dot{\boldsymbol{p}}(\boldsymbol{q}, \dot{\boldsymbol{q}})}_{=0} \\ &= -\boldsymbol{L}(\underbrace{\boldsymbol{z} + \boldsymbol{p}(\boldsymbol{q}, \dot{\boldsymbol{q}})}_{\hat{\tau}_{ext}}) + \boldsymbol{L}(\boldsymbol{C}(\boldsymbol{q}, \dot{\boldsymbol{q}}) + \boldsymbol{G}(\boldsymbol{q}) + \boldsymbol{F}(\dot{\boldsymbol{q}}) - \boldsymbol{\tau}) \end{aligned} \tag{12}$$

According to (10) and (12), the structure of modified disturbance observer (MDO) for external torque estimation is shown in Fig.2.

Proof: According to the definition of the observer error $\boldsymbol{s} = \boldsymbol{\tau}_{ext} - \hat{\boldsymbol{\tau}}_{ext}$, its dynamic becomes:

$$\dot{\boldsymbol{s}} = \dot{\boldsymbol{\tau}}_{ext} - \dot{\hat{\boldsymbol{\tau}}}_{\boldsymbol{ext}} = \dot{\boldsymbol{\tau}}_{ext} - (\dot{\boldsymbol{z}} + \dot{\boldsymbol{p}}(\boldsymbol{q}, \dot{\boldsymbol{q}})) \tag{13}$$

From (1) and (11), the derivative of the auxiliary variable $\boldsymbol{z}$ can be written as:

$$\begin{aligned} \dot{\boldsymbol{z}} &= -\boldsymbol{L}(\boldsymbol{z} + \boldsymbol{p}(\boldsymbol{q}, \dot{\boldsymbol{q}})) + \boldsymbol{L}(\boldsymbol{\tau}_{ext} - \boldsymbol{D}(\boldsymbol{q})\ddot{\boldsymbol{q}}) \\ &= \boldsymbol{L}(\boldsymbol{\tau}_{ext} - \hat{\boldsymbol{\tau}}_{ext}) - \boldsymbol{L}\boldsymbol{D}(\boldsymbol{q})\ddot{\boldsymbol{q}} \end{aligned} \tag{14}$$

By considering (12) and (14), the error dynamics (13) can be represented as follows:

$$\dot{\boldsymbol{s}} = \dot{\boldsymbol{\tau}}_{ext} - \boldsymbol{L}\boldsymbol{s} + (\boldsymbol{L}\boldsymbol{D}(\boldsymbol{q})\ddot{\boldsymbol{q}} - \dot{\boldsymbol{p}}(\boldsymbol{q}, \dot{\boldsymbol{q}})) \tag{15}$$

To eliminate the dependency of the observer error dynamics on the acceleration measurement $\ddot{\boldsymbol{q}}$, the assumption (11) should be held.

$$\begin{aligned} \dot{\boldsymbol{p}}(\boldsymbol{q}, \dot{\boldsymbol{q}}) &= (\partial \boldsymbol{p}(\boldsymbol{q}, \dot{\boldsymbol{q}})/\partial \boldsymbol{q})\dot{\boldsymbol{q}} + (\partial \boldsymbol{p}(\boldsymbol{q}, \dot{\boldsymbol{q}})/\partial \dot{\boldsymbol{q}})\ddot{\boldsymbol{q}} \\ &= \boldsymbol{L}\boldsymbol{D}(\boldsymbol{q})\ddot{\boldsymbol{q}} \end{aligned} \tag{16}$$

Therefore, $\partial \boldsymbol{p}(\boldsymbol{q}, \dot{\boldsymbol{q}})/\partial \boldsymbol{q} = 0$ must be satisfied and $\boldsymbol{p}(\boldsymbol{q}, \dot{\boldsymbol{q}})$ becomes a function of $\dot{\boldsymbol{q}}$, the following equation can be obtained:

$$\boldsymbol{L} = (\partial \boldsymbol{p}(\boldsymbol{q}, \dot{\boldsymbol{q}})/\partial \dot{\boldsymbol{q}})\boldsymbol{D}^{-1}(\boldsymbol{q}) = \boldsymbol{X}\boldsymbol{D}^{-1}(\boldsymbol{q}) \tag{17}$$

$$\boldsymbol{p}(\boldsymbol{q}, \dot{\boldsymbol{q}}) = (\partial \boldsymbol{p}(\boldsymbol{q}, \dot{\boldsymbol{q}})/\partial \dot{\boldsymbol{q}})\dot{\boldsymbol{q}} = \boldsymbol{X}\dot{\boldsymbol{q}} \tag{18}$$

where $\boldsymbol{X}$ is a constant diagonal and positive-definite matrix, which is the gain matrix of the MDO to be designed.

Error dynamics (15) can be simplified as follows:

$$\dot{\boldsymbol{s}} = \dot{\boldsymbol{\tau}}_{ext} - \boldsymbol{L}\boldsymbol{s} \tag{19}$$

To analyze the stability of the error dynamics in (19), we consider the following Lyapunov function:

$$\boldsymbol{V} = \frac{1}{2}\boldsymbol{s}^T\boldsymbol{D}(\boldsymbol{q})\boldsymbol{s} \tag{20}$$

The derivative of the Lyapunov function (20) becomes:

$$\begin{aligned} \dot{\boldsymbol{V}} &= \boldsymbol{s}^T\boldsymbol{D}(\boldsymbol{q})\dot{\boldsymbol{s}} \\ &= \boldsymbol{s}^T\boldsymbol{D}(\boldsymbol{q})(\dot{\boldsymbol{\tau}}_{ext} - \boldsymbol{L}\boldsymbol{s}) \\ &= -\boldsymbol{s}^T\boldsymbol{D}(\boldsymbol{q})\boldsymbol{X}\boldsymbol{D}^{-1}(\boldsymbol{q})\boldsymbol{s} + \boldsymbol{s}^T\boldsymbol{D}(\boldsymbol{q})\dot{\boldsymbol{\tau}}_{ext} \end{aligned} \tag{21}$$

Considering that $\boldsymbol{X}$ is a constant diagonal and positive-definite matrix and $\boldsymbol{D}(\boldsymbol{q})$ is a symmetric, positive-definite matrix, it is clear that $\boldsymbol{D}(\boldsymbol{q})\boldsymbol{X}\boldsymbol{D}^{-1}(\boldsymbol{q})$ is also a positive definite matrix. Using Rayleigh inequality [39], the following inequalities can be obtained:

$$\lambda_{min}(\boldsymbol{X})\,\|\boldsymbol{s}\|^2 \le \boldsymbol{s}^T\boldsymbol{D}(\boldsymbol{q})\boldsymbol{X}\boldsymbol{D}^{-1}(\boldsymbol{q})\boldsymbol{s} \le \lambda_{max}(\boldsymbol{X})\,\|\boldsymbol{s}\|^2 \tag{22}$$

$$\boldsymbol{s}^T\boldsymbol{D}(\boldsymbol{q})\dot{\boldsymbol{\tau}}_{ext} \le \|\boldsymbol{s}\|\,\|\boldsymbol{D}(\boldsymbol{q})\|\,\|\dot{\boldsymbol{\tau}}_{ext}\| \tag{23}$$

where $\lambda_{min}(\boldsymbol{X})$ and $\lambda_{max}(\boldsymbol{X})$ are the minimum and maximum eigenvalues of matrix $\boldsymbol{X}$, respectively. It should be remarked that $0 < \lambda_{min}(\boldsymbol{X}) \le \lambda_{max}(\boldsymbol{X})$ is satisfied owing to the properties of the positive definite matrix $\boldsymbol{X}$.

Combining (22) and (23) with (21) yields:

$$\dot{\boldsymbol{V}} \le -\lambda_{min}(\boldsymbol{X})\,\|\boldsymbol{s}\|^2 + \|\boldsymbol{s}\|\,\|\boldsymbol{D}(\boldsymbol{q})\|\,\|\dot{\boldsymbol{\tau}}_{ext}\| \tag{24}$$

Theorem 1: If the external joint torque is constant, that is, $\dot{\boldsymbol{\tau}}_{ext} = 0$, the observer error $\boldsymbol{s}$ converges asymptotically to zero and $\hat{\boldsymbol{\tau}}_{ext}$ approaches the external joint torque $\boldsymbol{\tau}_{ext}$.

Proof: $\dot{V}$ in (24) can be simplified as follows:

$$\dot{V} \leq -\lambda_{min}(\boldsymbol{X}) \|\boldsymbol{s}\|^2 \leq 0 \tag{25}$$

From equation (25), we can conclude that the derivative of the Lyapunov function $\dot{V}$ is a negative-definite function. Also, the error dynamics (19) becomes $\dot{\boldsymbol{s}} + \boldsymbol{L}\boldsymbol{s} = 0$, and its solution can be written as:

$$\boldsymbol{s} = Ce^{-\boldsymbol{L}t} \leq Ce^{-\lambda_{\min}(\boldsymbol{X})t/d_2} \tag{26}$$

where C is a constant. Note that $\|\boldsymbol{L}\| \geq \lambda_{\boldsymbol{min}}(\boldsymbol{X})/d_2$ is satisfied. Then, the error dynamics is asymptotically stable.

Theorem 2: If the external joint torque is time varying and its time derivative is bounded by a positive constant ε, that is, $\|\dot{\boldsymbol{\tau}}_{ext}\| \leq \varepsilon(\varepsilon > 0)$ the observer error $\boldsymbol{s}$ converges with an exponential rate in a finite time and bounded uniformly.

Proof: The inequality (24) can be represented as follows:

$$\begin{aligned}\dot{V} &\leq -\lambda_{min}(\boldsymbol{X}) \|\boldsymbol{s}\|^2 + \|\boldsymbol{s}\| \|\boldsymbol{D}(\boldsymbol{q})\| \|\dot{\boldsymbol{\tau}}_{ext}\| \\ &= -\|\boldsymbol{s}\| (-\lambda_{min}(\boldsymbol{X}) \|\boldsymbol{s}\| + \|\boldsymbol{D}(\boldsymbol{q})\| \|\dot{\boldsymbol{\tau}}_{ext}\|) \\ &\leq -\|\boldsymbol{s}\| (-\lambda_{min}(\boldsymbol{X}) \|\boldsymbol{s}\| + \|\boldsymbol{D}(\boldsymbol{q})\| \varepsilon)\end{aligned} \tag{27}$$

From equation (27), it is seen that $\dot{V}$ is a negative-definite function if the following inequality (28) is satisfied:

$$-\lambda_{min}(\boldsymbol{X}) \|\boldsymbol{s}\| + \|\boldsymbol{D}(\boldsymbol{q})\| \varepsilon > 0 \tag{28}$$

Apparently, the solution boundedness of the error dynamics (19) is guaranteed in the region (29) and its solution can be expressed as the from (30).

$$\dot{V} < -\|\boldsymbol{s}\| < 0, \quad \forall \|\boldsymbol{s}\| \in \boldsymbol{D} = \left\{ \|\boldsymbol{s}\| > \frac{\|\boldsymbol{D}(\boldsymbol{q})\| \varepsilon}{\lambda_{min}(\boldsymbol{X})} \right\} \tag{29}$$

$$\boldsymbol{s} < Ce^{-\lambda_{min}(\boldsymbol{X})t/d_2} + \frac{\|\boldsymbol{D}(\boldsymbol{q})\| \varepsilon}{\lambda_{min}(\boldsymbol{X})} \tag{30}$$

Therefore, the observer error converges at an exponential rate in a finite time and into a bounded region $\boldsymbol{D}$. From (30), the convergence speed is governed by $\lambda_{min}(\boldsymbol{X})$. The decay rate of the observer error increases when $\lambda_{min}(\boldsymbol{X})$ is larger, ultimately leading to a faster convergence speed. $\lambda_{min}(\boldsymbol{X})$ is determined by the selection of the gain matrix $\boldsymbol{X}$. Hence, the observer design can be transformed into the selection of the gain matrix.

For the fault detection of the force sensor, it is assumed that $\|\boldsymbol{\tau}_{ext}\| \leq \varepsilon(\varepsilon > 0)\cdot$ in Theorem 2 is satisfied and the inequality (30) can be rewritten as follows:

$$\boldsymbol{s} < Ce^{-\lambda_{min}(\boldsymbol{X})t/d_2} + \frac{\|\boldsymbol{D}(\boldsymbol{q})\| \varepsilon}{\lambda_{min}(\boldsymbol{X})} \leq C + \frac{\|\boldsymbol{D}(\boldsymbol{q})\| \varepsilon}{\lambda_{min}(\boldsymbol{X})} = \sigma \tag{31}$$

where σ denotes a constant determined by the $\boldsymbol{X}$, ε, and $\boldsymbol{D}(\boldsymbol{q})$. The external force can be precisely measured by the force sensor while working in a good condition and the equivalent joint torque $\boldsymbol{\tau}_m$ caused by the external force is equal to the actual torque $\boldsymbol{\tau}_{ext}$. Hence, the following inequality holds:

$$\boldsymbol{s} = \boldsymbol{\tau}_m - \hat{\boldsymbol{\tau}}_{ext} < \sigma(\boldsymbol{\tau}_m = \boldsymbol{\tau}_{ext}) \tag{32}$$

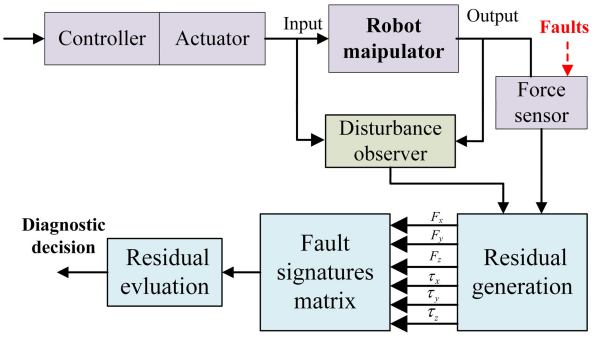

FIGURE 3. Schematic diagram of disturbance observer-based fault detection.

TABLE 1. Fault signatures matrix.

f/R	F_x	F_y	F_z	τ_x	τ_y	τ_z
f_1	1	0	0	0	0	0
f_2	0	1	0	0	0	0
f_3	0	0	1	0	0	0
f_4	0	0	0	1	0	0
f_5	0	0	0	0	1	0
f_6	0	0	0	0	0	1

Accordingly, the inequality (32) in Cartesian space can be formulated as:

$$\boldsymbol{s}_c = \boldsymbol{F}_m - \hat{\boldsymbol{F}}_{ext} < \boldsymbol{\sigma}_c(\boldsymbol{F}_m = \boldsymbol{F}_{ext}) \tag{33}$$

where $\boldsymbol{F}_m$, $\boldsymbol{F}_{ext}$, and $\hat{\boldsymbol{F}}_{ext}$ are the measured, actual, and estimated force on end effector, respectively; $\boldsymbol{s}_c$ is the estimated error of external force. $\boldsymbol{\sigma}_c$ is the threshold to be designed. The sensor fault can be detected by the residuals between sensor measurement and estimated outputs, which is defined as $\boldsymbol{R} = \left|\boldsymbol{F}_m - \hat{\boldsymbol{F}}_{ext}\right|$. The detection mechanism of the sensor fault by using inequality (33) can be presented as follows:

$$\boldsymbol{f} = \begin{cases} 0, & |\boldsymbol{s}_c| < \sigma_c \\ 1, & otherwise \end{cases} \tag{34}$$

where $\boldsymbol{f}$ denotes the fault signature. $\boldsymbol{f} = 0$ indicates the residual within the threshold range and the sensor works in good condition. $\boldsymbol{f} = 1$ indicates that the residual goes beyond the threshold and the sensor fault may occur due to radiation damage. The schematic diagram of the disturbance observer-based fault detection is shown in Fig. 3.

The fault signature matrix for the residuals is shown in Table 1.

Furthermore, the estimated external force can be obtained by using the following relationship:

$$\hat{\boldsymbol{\tau}}_{\boldsymbol{ext}} = \boldsymbol{J}^T \hat{\boldsymbol{F}}_{\boldsymbol{ext}} \tag{35}$$

where $\boldsymbol{J}^T$ denotes the transposed matrix of the Jacobian. $\hat{\boldsymbol{F}}_{\boldsymbol{ext}}$ is defined as follows:

$$\hat{\boldsymbol{F}}_{\boldsymbol{ext}} = [\hat{F}_x, \hat{F}_y, \hat{F}_z, \hat{\tau}_x, \hat{\tau}_y, \hat{\tau}_z]^T \tag{36}$$

Finally, the external force on the end-effector can be computed by the following equations:

$$\hat{\boldsymbol{F}}_{ext} = (\boldsymbol{J}^T)^{-1}\hat{\boldsymbol{\tau}}_{ext} \tag{37}$$

where $(\boldsymbol{J}^T)^{-1}$ is the inverse matrix of the manipulator Jacobian.

IV. NUMERICAL SIMULATIONS

In this section, simulations were conducted on Simulink/MATLAB to illustrate the effectiveness of the proposed estimation scheme. The dynamic parameters of the Six-DOF Kinova Jaco^2 robot manipulator used in the simulation were obtained by the dynamic parameter identification methods [40], [41]. These parameters are listed in Appendix. To show the disturbance attenuation ability and the tracking performance of the proposed scheme, the proposed scheme is compared with the conventional PD controller and the adaptive bias radial basis function neural network (RBFNN) controller [24].

The gains of the conventional PD controller are chosen as:

$$K_p = diag\{40, 40, 40, 20, 20, 20\} \tag{38}$$
$$K_d = diag\{8, 8, 8, 0.4, 0.4, 0.4\} \tag{39}$$

The gains of the adaptive bias RBFNN controller are chosen as:

$$K_1 = diag\{10, 10, 10, 5, 5, 5\} \tag{40}$$
$$K_2 = diag\{5, 5, 5, 2.5, 2.5, 2.5\} \tag{41}$$

The input number of adaptive RBFNN $m = 18$, the number of hidden layer nodes $P = 7$; The center of the receptive field of Gaussian functions are selected as $c = [-1.5, -1, -0.5, 0, 0.5, 1, 1.5]_{18\times 7}$, and the width of Gaussian functions $b = 1$. In term of the adaptive law, the learning rate $\Gamma = diag\{8, 8, 8, 4, 4, 4\}$, the discontinuous switching constant $\delta = 0.001$, and the weight of the adaptive RBFNN controller $W = 14$.

The initial condition used for simulation is set as:

$$\boldsymbol{q}(0),\quad \dot{\boldsymbol{q}}(0),\ \ddot{\boldsymbol{q}}(0),\ \boldsymbol{q}_d(0),\ \dot{\boldsymbol{q}}_d(0) = 0 \tag{42}$$
$$z = [0, 0, 0, 0, 0, 0]^T \tag{43}$$

To evaluate the performance of the proposed control strategy and force estimation method. The gain matrix used in the simulation are given in Table 2. The desired position trajectories for the Kinova Jaco^2 manipulator are depicted in Fig. 4. The step torque and composite sinusoidal torque are assumed to be joint disturbance torque.

A step torque of 10 Nm was applied to all the joint 1-6 to analyze the step response of the proposed observer, which simulates the rapidly changing disturbance. The estimation results of the step disturbance torque for different gain matrices are depicted in Fig. 5. The settling times of the 2% criterion for the estimated external torque are listed in Table 3.

It can be observed that the MDO can exactly estimate the sudden change of the disturbance torque and the gain matrix $\boldsymbol{X}_3$ provides the fastest convergence speed in the response

TABLE 2. The selection for the gain matrix $\boldsymbol{X}$.

Parameter	Value
$\boldsymbol{X}_1$	$diag\{[1;1;1;2;2;2]\}$
$\boldsymbol{X}_2$	$diag\{[10;10;10;20;20;20]\}$
$\boldsymbol{X}_3$	$diag\{[100;100;100;200;200;200]\}$

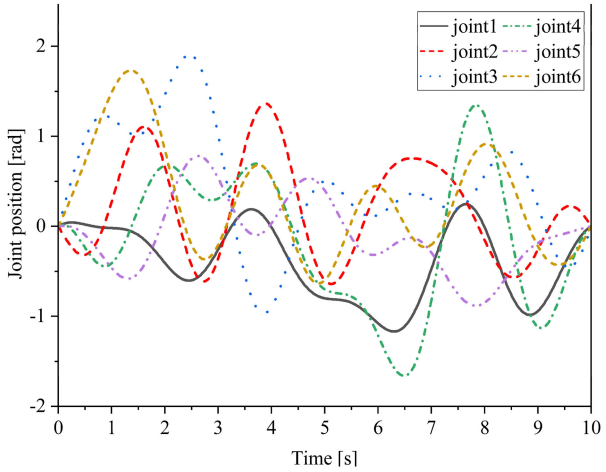

FIGURE 4. The desired position trajectories for Kinova Jaco^2 manipulator.

of the step external torque. Moreover, the estimation errors converge to zero and the estimated torque by using MDO approaches the actual joint torque while the disturbance torques remain constant from 1 to 6 s. This confirms the correctness of the analysis in the Theorem 1.

The position tracking control is performed with and without MDO compensation under the gain matrix $\boldsymbol{X}_3$ and the same controller gain parameter. The tracking performances of the conventional PD control and the adaptive bias RBFNN control with and without MDO compensation are compared in Fig. 6. The tracking error are showed in Fig. 7. From Figs. 6 and 7, the adaptive bias RBFNN control scheme presents the superior tracking control performance on the tracking precision and strongest property to uncertain terms compared with the conventional PD control scheme. However, the adaptive bias RBFNN control scheme has still the steady tracking error in the presence of disturbance. On the other hand, both the conventional PD controller and the adaptive bias RBFNN controller with MDO compensation can significantly improve the position tracking performance and enhance the disturbance attenuation ability.

To further analyze the robustness performance of the position tracking and the torque estimation for a fast-varying disturbance torque. A composite sinusoidal torque with $\tau = 10\sin(2\pi t)+\sin(20\pi t)$ is applied to all the joint 1-6 from t=1 to 9 s. Fig. 8 shows the estimation results of the composite sinusoidal disturbance torque under the different gain matrices. The corresponding tracking errors are shown in Fig 9. As shown in Figs. 8 and 9, the MDO can still estimate the fast-varying disturbance torque with bounded tracking errors. The larger (smaller) eigenvalue of the matrix may lead to the

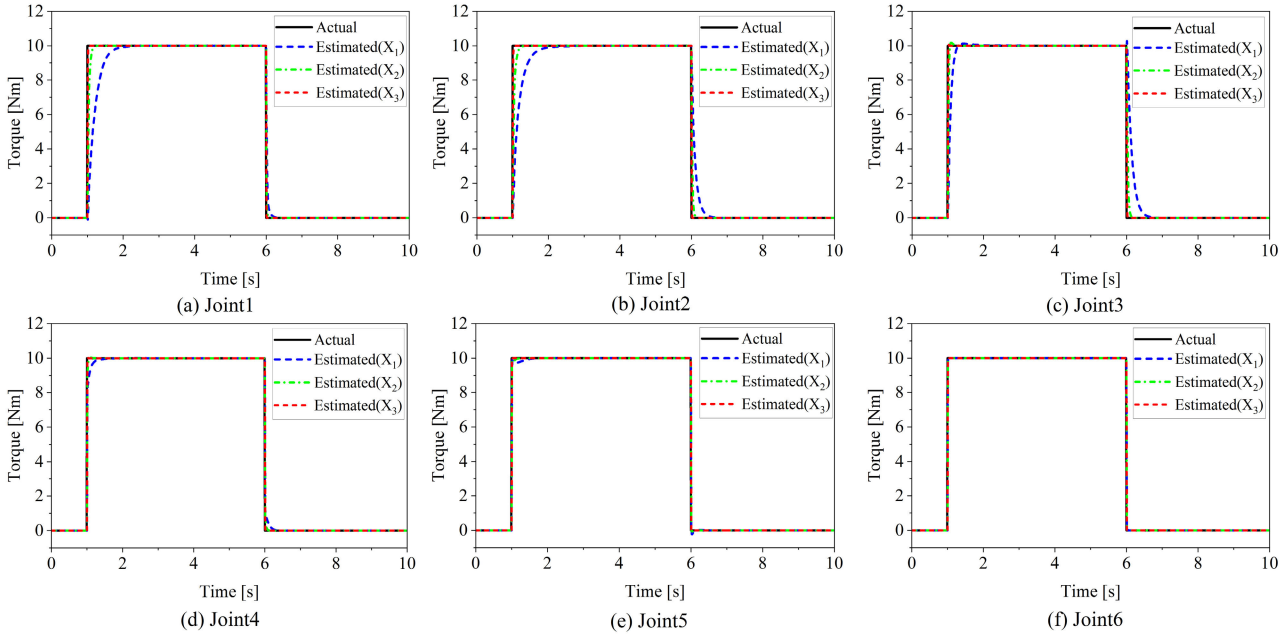

FIGURE 5. Estimation of step disturbance torque applied on all joints: (a) - (f) corresponding to the joint 1- joint 6.

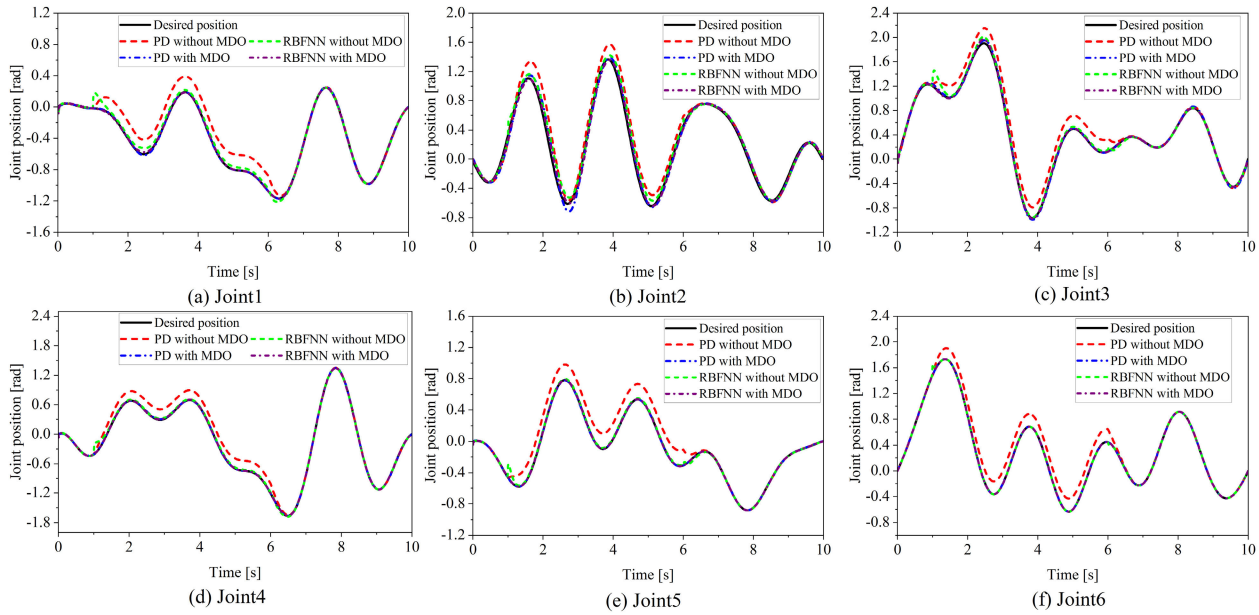

FIGURE 6. Tracking performances with and without MDO (step disturbance torque): (a) - (f) corresponding to the joint 1- joint 6.

smaller (larger) tracking error and a larger rate of change in the disturbance torque results in an increased tracking error. These results support the analysis in Theorem 2.

Similarly, the joint position tracking control is performed with the same controller parameter of the step disturbance torque simulation. The joint position tracking performances of each joints with and without MDO compensation are shown in Fig. 10. The tracking error are showed in Fig. 11. It can be clearly seen that the conventional PD controller under the fast-varying torque disturbance shows a relatively stable system but has a large tracking error. Compared with the conventional PD controller, the adaptive bias RBFNN controller provides a relatively good tracking performance and results in much smaller tracking error. However, both the conventional PD controller and the adaptive bias RBFNN controller cannot completely cancel the effect of disturbances due to lack of the feedforward compensation. The MDO can effectively suppress the fast-varying disturbances and greatly reduces the tracking error of each joints caused by these disturbances. The composite controller integrated with MDO compensation significantly improve the tracking performance under the disturbance and achieve strong robustness against torque disturbances.

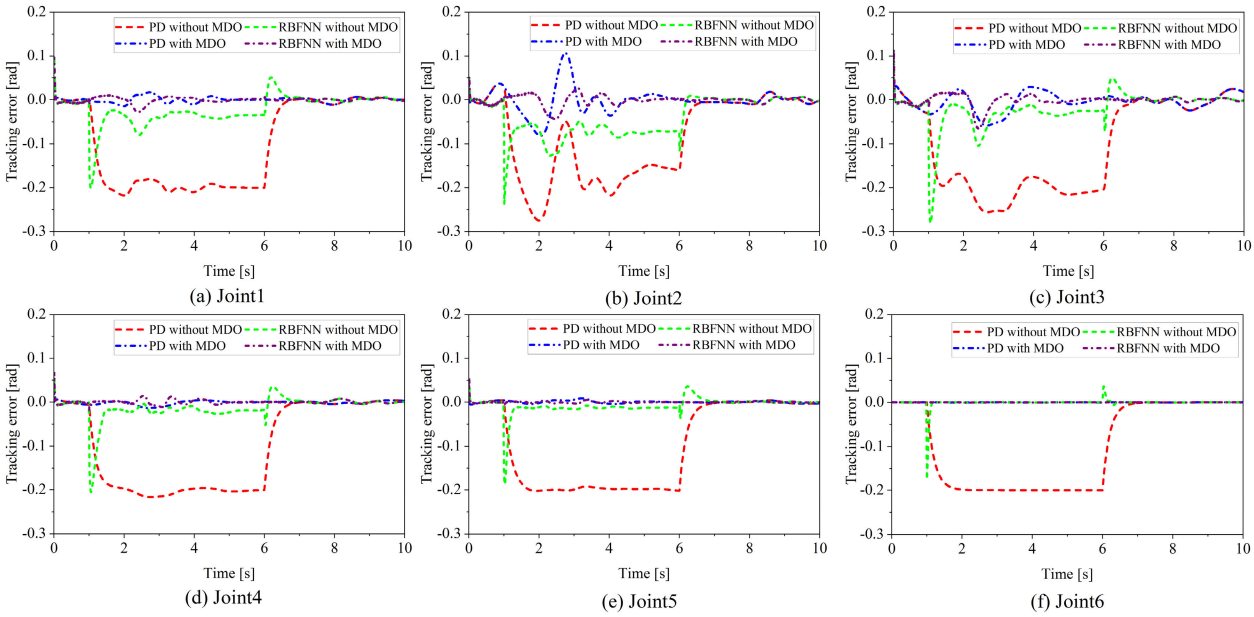

FIGURE 7. Tracking errors with and without MDO (step disturbance torque): (a) - (f) corresponding to the joint 1- joint 6.

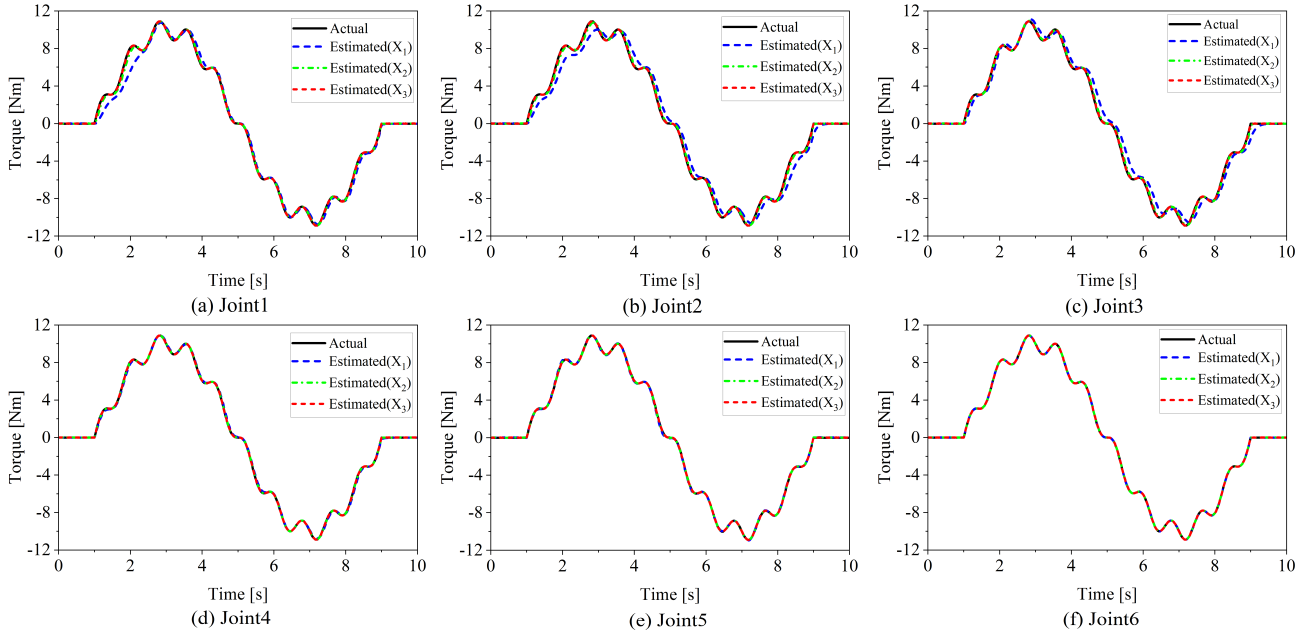

FIGURE 8. Estimation of the composite sinusoidal disturbance torque applied on all joints: (a) - (f) corresponding to the joint 1- joint 6.

V. EXPERIMENTS AND DISCUSSIONS

The experiment for validating the proposed observer was performed on a Six-DOF Kinova Jaco^2 manipulator, which is a lightweight robot with revolute joints, as shown in Fig. 12. Integrated encoders and torque sensors are embedded in each joint for position, velocity and torque measurements. The joint of the manipulator is controlled by the Kinova SDK developed in the Matlab/Simulink. The sampling frequency is 100Hz. The Denavit-Hartenberg (DH) table for the manipulator are given in Table 4. The controller gain parameters for the manipulator are set as the same in (38) and (39). The gain matrix was chosen as $\boldsymbol{X}_3$.

A. EXPERIMENT 1: EXTERNAL TORQUE ESTIMATION WITH A FIXED POSITION

To illustrate the effectiveness of the proposed method for the external torque estimation with a fixed position, the load (a steel ball of 1 Kg) was applied to the manipulator end-effector as an external disturbing force. The load is regarded as a constant force in the Z direction. Accordingly, the disturbance torque caused by the load was exerted on each joint. The disturbance torque was changed by exerting and removing the load. The load is placed on the end effector from t = 5.0 to 15.4s and 25.8 to 35.3s while the joint position is keeping stable at $\boldsymbol{q} = [-\pi/4; \pi; \pi/2; 0; 0; 0]$ rad, as shown in Fig. 12.

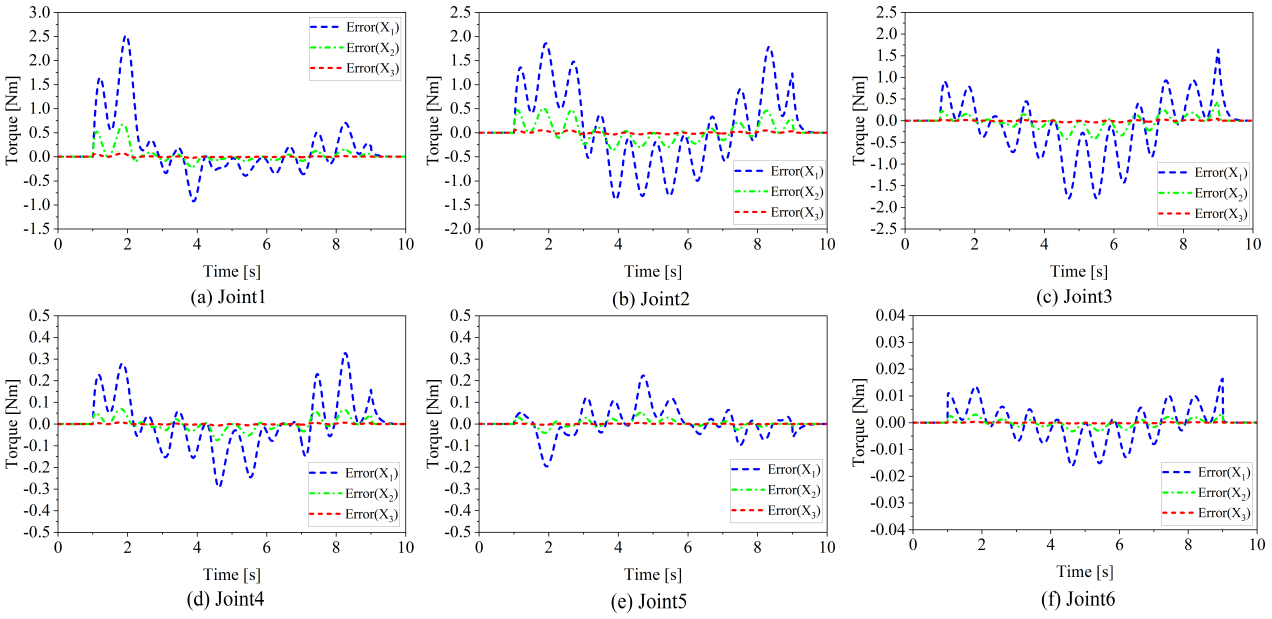

FIGURE 9. Tracking error of MDO (composite sinusoidal disturbance torque): (a) - (f) corresponding to the joint 1- joint 6.

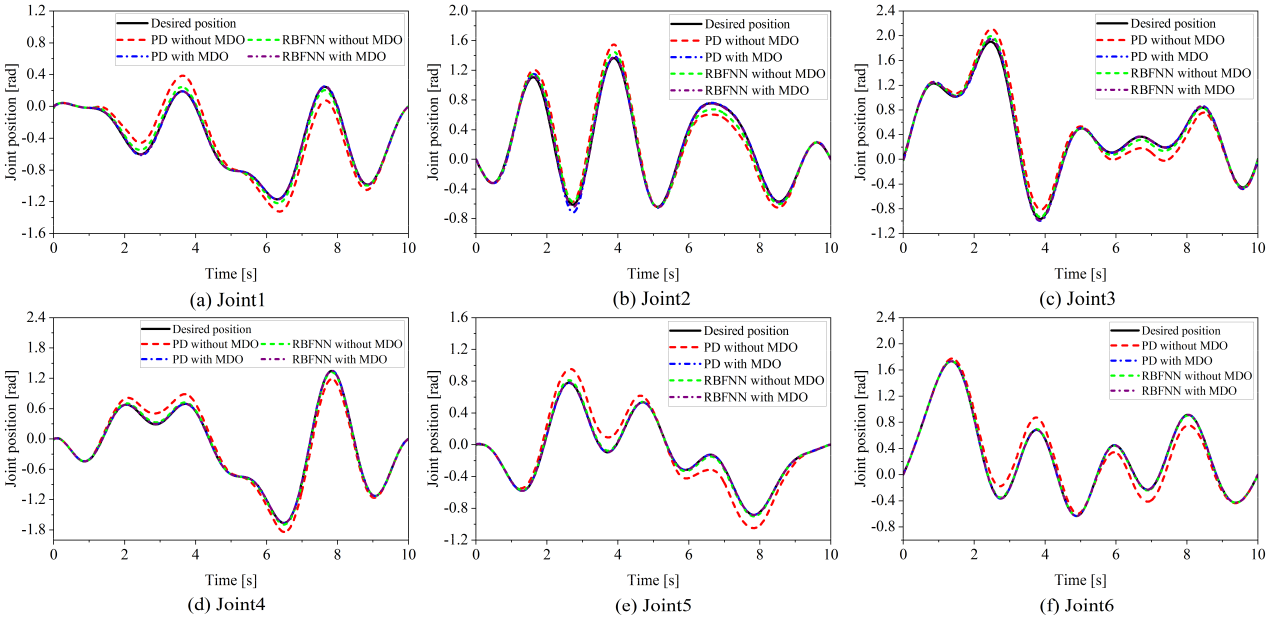

FIGURE 10. Tracking performances with and without MDO (the composite sinusoidal disturbance torque): (a) - (f) corresponding to the joint 1- joint 6.

TABLE 3. Settling time of 2% criteria for the estimated external torque.

Joint	X_1 [s]	X_2 [s]	X_3 [s]
1	0.77	0.15	0.03
2	0.79	0.19	0.04
3	0.26	0.07	0.03
4	0.22	0.05	0.02
5	0.27	0.07	0.02
6	0.03	0.02	0.01

TABLE 4. DH parameters for Kinova Jaco^2 manipulator.

Link	α_i(rad)	a_i(m)	d_i(m)	θ_i(rad)
1	π/2	0	0.2755	q1
2	π	0.41	0	q2
3	π/2	0	-0.0098	q3
4	π/2	0	-0.2814	q4
5	π/2	0	0	q5
6	π	0	-0.2341	q6

The estimated joint torque was compared with the actual measurement (obtained by the joint torque sensor). Fig. 13 shows the estimation results of the external disturbance torques exerted on the joints. The results in Fig. 13 indicate that the

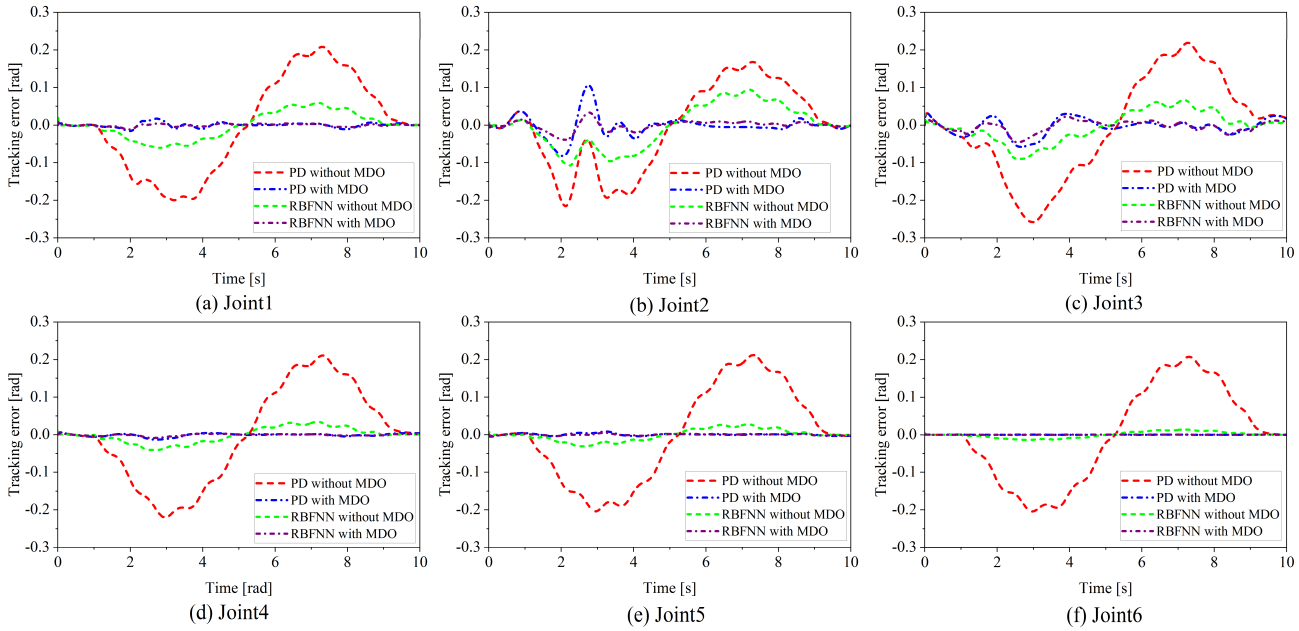

FIGURE 11. Tracking errors with and without MDO (the composite sinusoidal disturbance torque): (a) - (f) corresponding to the joint 1- joint 6.

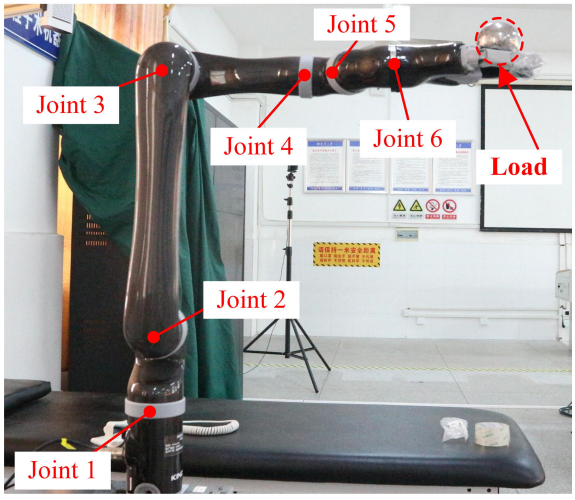

FIGURE 12. Six-DOF Kinova Jaco^2 manipulator.

estimated external torque can rapidly and precisely follow the actual torque. It should be noted that the external torques produced by the load were only exerted on joints 2, 3, and 5 in this case.

B. EXPERIMENT 2: EXTERNAL TORQUE ESTIMATION WITH A TRACKING TASK

To evaluate the performance of the proposed method for the external torque estimation with a tracking task, the manipulator was controlled to execute the tracking task while the load was placed on the end effector from t = 1.1 to 8.8 s and 20.8 to 28.1 s. Fig. 14 shows the motion of the manipulator for the tracking task. The position and velocity of all the joints in the joint space are shown in Fig. 15(a) and Fig. 15(b). Correspondingly, the trajectory of the end effector in Cartesian space is shown in Fig. 15(c). Note that the joints 4 to 6 are still at a fixed position so that the load (the steel ball) is always placed on the end-effector during the motion.

Fig. 16 shows the estimation results of the external disturbance torques on each joint in this case. As can be seen, the estimation results provide relatively accurate approximation of the actual external torque in magnitude and time response. A spike occurs in the actual torque when the joint velocity is reversed, which is mainly caused by the nonlinear friction. Therefore, it is reasonable to infer that the MDO can effectively predict the unknown disturbance torques when the manipulator performs a tracking task.

C. EXPERIMENT 3: ELASTIC FORCE ESTIMATION ON THE END EFFECTOR

To highlight the effectiveness of the proposed method, another experiment of the elastic force estimation was performed and compared with the extended state observer (ESO) estimation method [9]. A six-axis force sensor (Robotiq, FT300) was used to measure the actual force exerted on the end effector. A spring with an elastic coefficient of 1.16 N/mm was installed between the end effector and the force sensor. The end-effector was commanded to move up and down vertically, and the elastic force generated by the spring was changed with a 5 second cycle, as shown in Fig. 17. The gain parameters of the ESO parameterized by using the pole placement technique [42] are listed in Table 5.

The estimated joint torques by using the proposed and ESO-based methods were compared with the actual torques in joint space, as shown in Fig. 18. According to the estimated joint torques (see Fig. 18), the corresponding estimation of the external forces can be computed by Eq. (37). Fig. 19 shows the measurement of the external forces and the estimation of external forces in Cartesian space, where

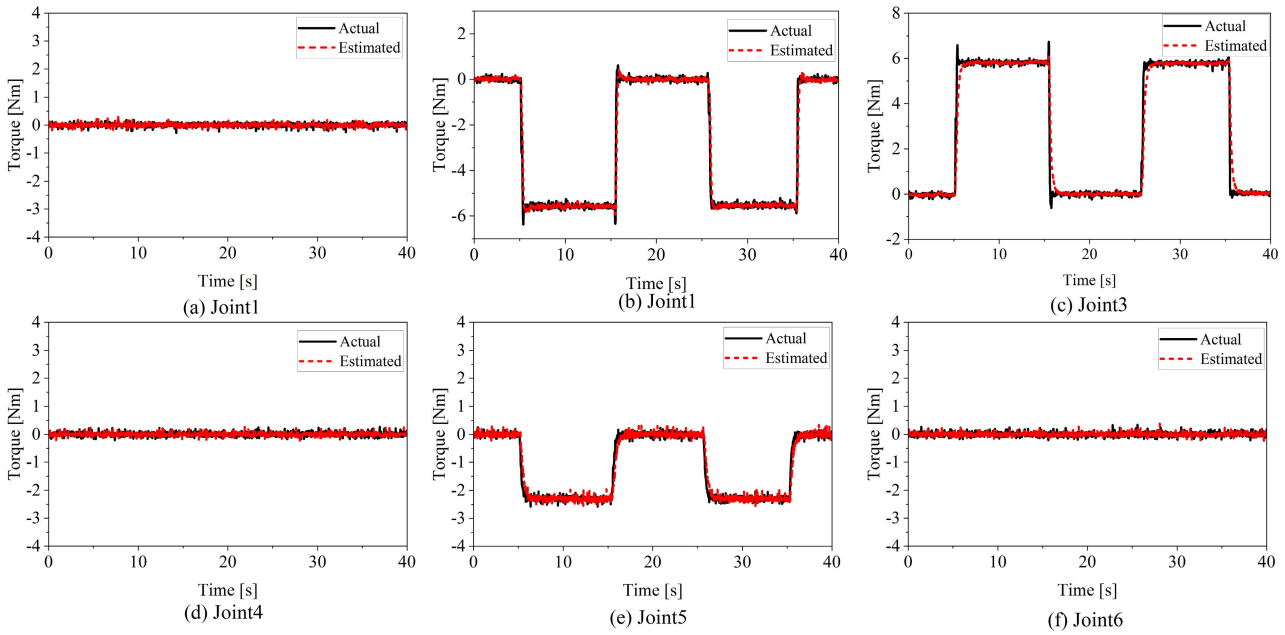

FIGURE 13. Estimation results of external torques with a fixed position: (a) - (f) corresponding to the joint 1- joint 6.

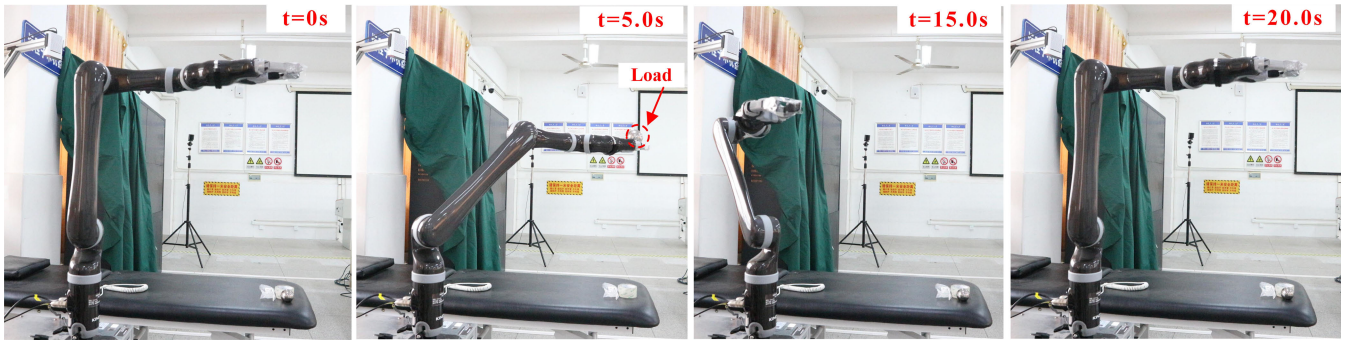

FIGURE 14. The movement of robot manipulator for the tracking task.

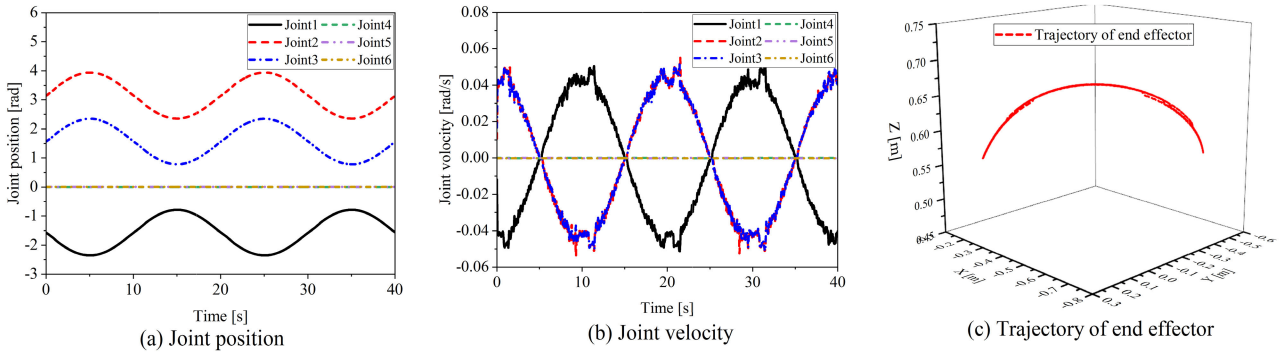

FIGURE 15. The joint position, velocity in joint space and trajectory of end effector in Cartesian space: (a) joint position, (b) joint velocity, (c) trajectory of end effector.

the measured forces were obtained by using the force sensor (Robotiq, FT300). The estimation errors of the external force induced by the proposed and ESO methods in the X-Y-Z direction are shown in Fig. 20. As it is shown in Fig. 20, the estimation errors of the proposed method in the X-Y-Z direction are bounded within ±0.5 N, ±2 N and ±3 N, respectively.

Moreover, the performance of the proposed scheme was quantitatively evaluated by the root-mean-square (RMS) error between the measurement and the estimation, which can be expressed as follows [43]:

$$\varepsilon_{RMS} = \sqrt{\frac{1}{N}\sum_{i=1}^{N}(\tau_{mi} - \tau_{ei})^2} \tag{44}$$

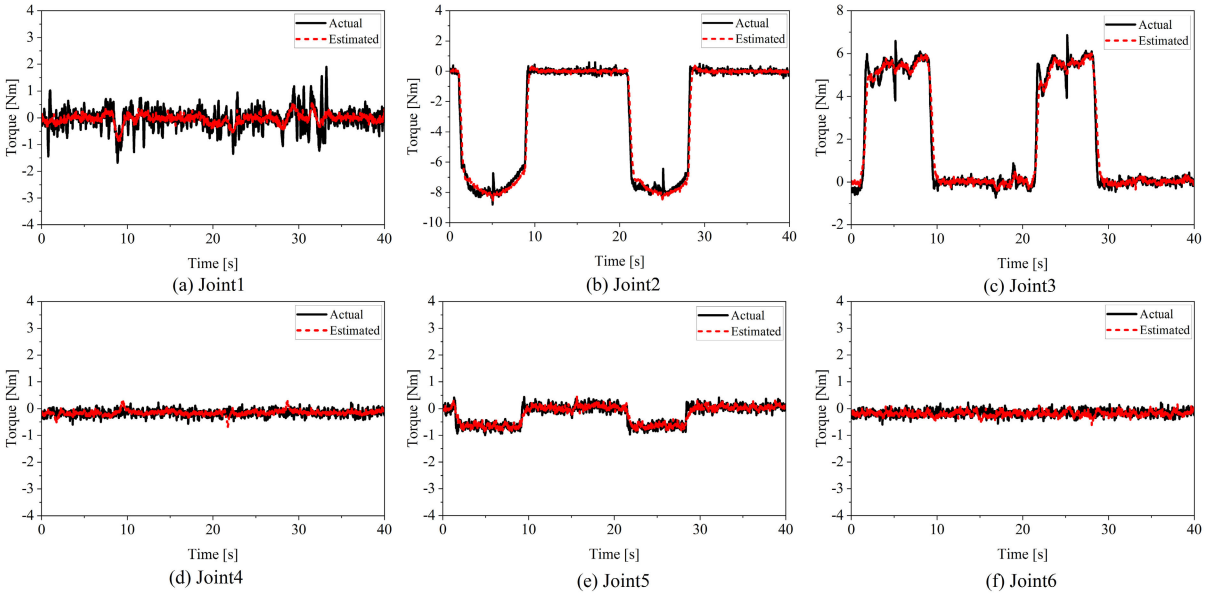

FIGURE 16. Estimation results of external torques with the tracking task: (a) - (f) corresponding to the joint 1- joint 6.

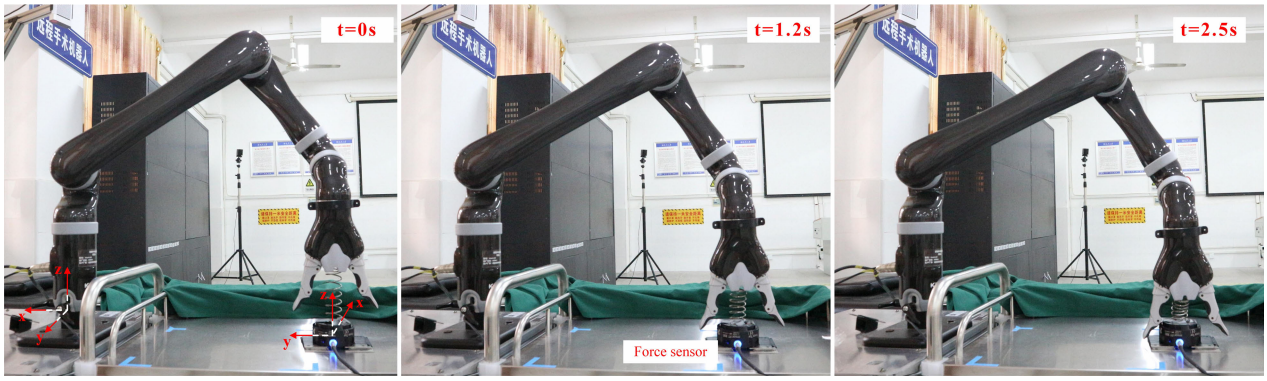

FIGURE 17. Experiment for the elastic force estimation on the end effector.

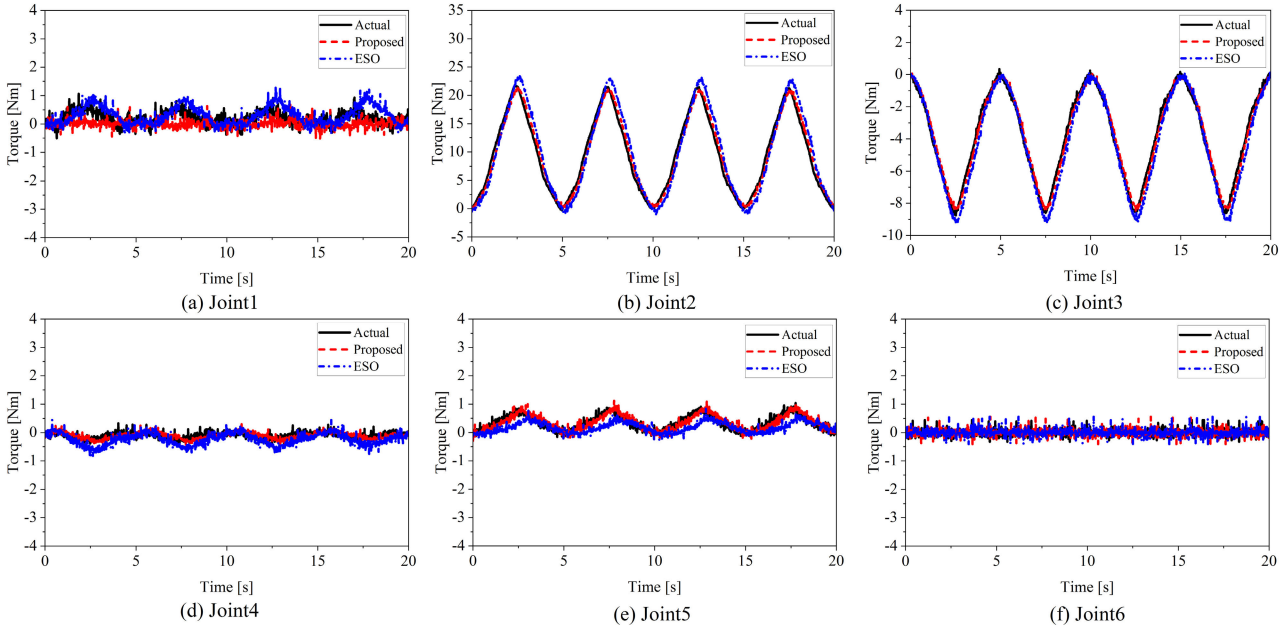

FIGURE 18. Comparison between the estimated and actual torque in all joints: (a) - (f) corresponding to the joint 1- joint 6.

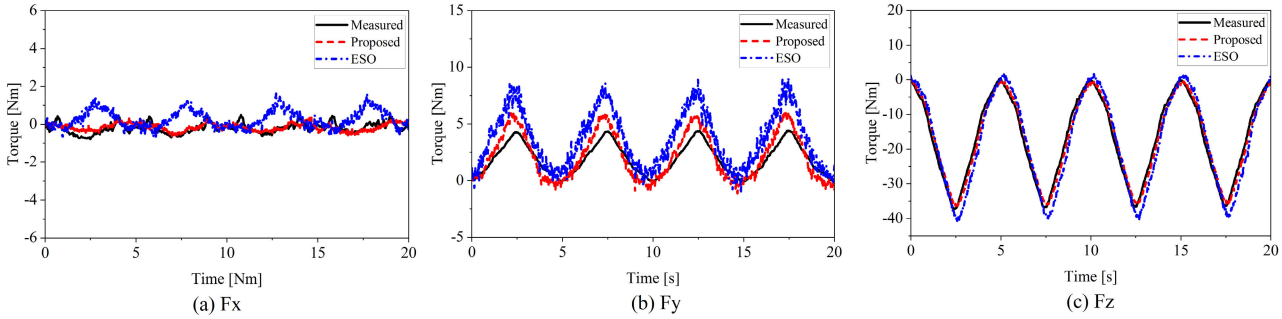

FIGURE 19. Comparison between the measured and estimated force on the end effector: (a) - (c) corresponding to the external force in X-Y-Z direction.

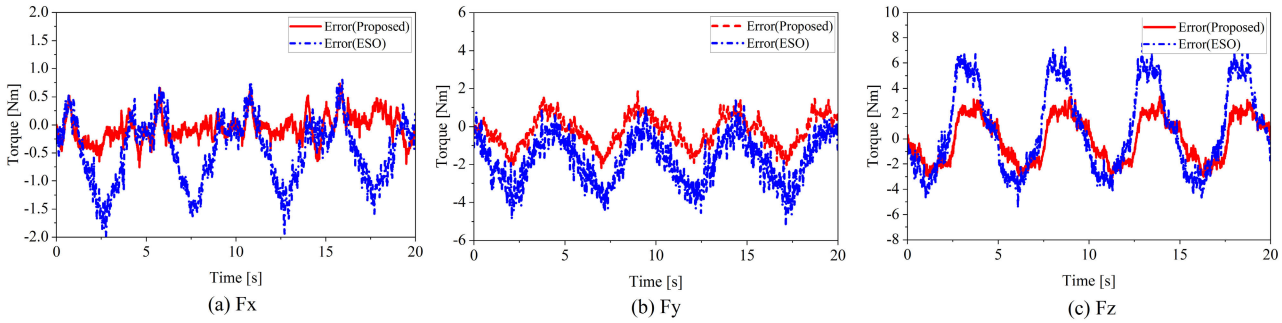

FIGURE 20. Estimation error of external force induced by the proposed and ESO method: (a) - (c) corresponding to the estimation error in X-Y-Z direction.

TABLE 5. The gain parameters of ESO.

Parameter	Value
β_1	$diag\{24,24,24,12,12,12\}$
β_2	$diag\{192,192,192,48,48,48\}$
β_3	$diag\{512,512,512,64,64,64\}$

TABLE 6. RMS errors of torque estimation for the experimental validation.

Joint#	Fixed position [Nm]	Tracking task [Nm]	Elastic force [Nm]	
			Proposed	ESO
Joint1	0.06	0.33	0.20	0.26
Joint2	0.29	0.43	0.76	1.39
Joint3	0.46	0.50	0.45	0.61
Joint4	0.08	0.12	0.08	0.15
Joint5	0.17	0.15	0.09	0.21
Joint6	0.08	0.13	0.09	0.11
Sum	1.14	1.66	1.67	2.73

where τ_{mi} is the i^{th} sample of the measured value and τ_{ei} is the estimated value of torque /force at the i^{th} point. N represents the total number of samples. The RMS errors of the torque estimation for the experimental validation are summarized in Table 6. The RMS errors of external force estimation induced by the proposed and ESO methods are compared in Table 7.

These results indicate that the RMS errors of the proposed scheme are smaller than the ESO method and the proposed scheme is more effective in estimating the external force.

TABLE 7. The comparison of RMS error for external force estimation.

RMS[N]	Fx	Fy	Fz
Proposed	0.24	0.84	1.79
ESO	0.73	2.15	12.54

D. EXPERIMENT 4: FORCE SENSOR FAULT DETECTION

Similar to experiment 3, the final experiment was performed to illustrate the effectiveness of the proposed approach for fault detection. A broken connection of the signal was exerted on the force sensor to simulate a sensor fault, which can result in a sudden change in the measured value. Fig. 21 shows the measured and estimated external forces when the signal is disconnected at 7.7 s. As shown in Fig. 21, the estimated force output can track the actual sensor measurement in the X-Y-Z direction before sensor faults occur. However, the force sensor cannot measure the external force after a fault occurs, while the proposed observer is still effective in estimating the external force. The residuals between the estimated force outputs and the actual force outputs in the X-Y-Z direction are shown in Fig. 22. The detection thresholds for residuals in the X-Y-Z direction were set as ± 1 N, ± 2.5 N and ± 4 N, respectively. The residuals were within the thresholds in the absence of faults (before 7.7 s) and out of the thresholds once a fault occurred (after 7.7 s). Note that the residual signal in the X direction does not exceed its threshold because of the smaller external force in the X direction.

According to the decision mechanism (34) described in Section 3, the sensor fault signatures in the X-Y-Z direction can be obtained to detect the sensor fault. The fault signature

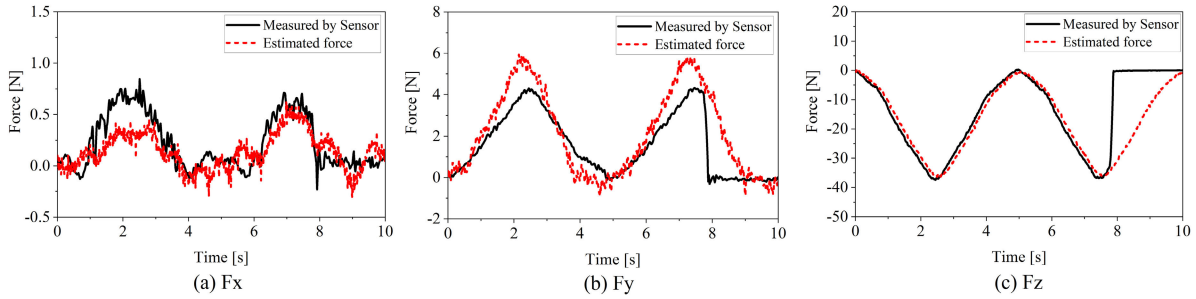

FIGURE 21. The measured and estimated force: (a) - (c) corresponding to the external force in X-Y-Z direction.

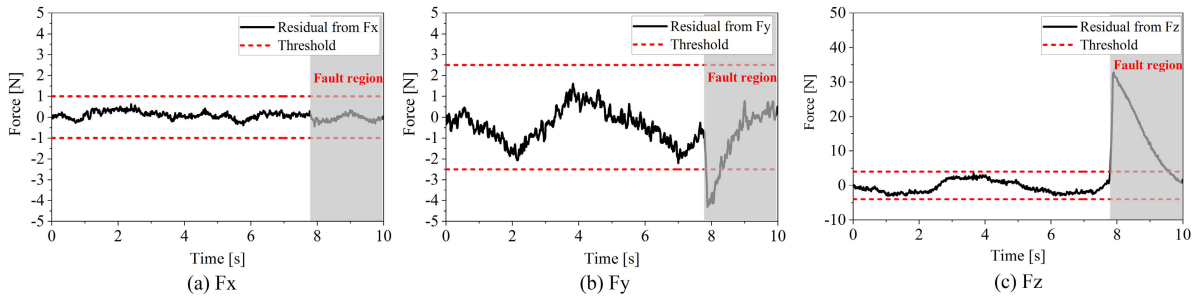

FIGURE 22. Residual and detection threshold for fault detection: (a) - (c) corresponding to the residual in X-Y-Z direction.

TABLE 8. Fault signature matrix for the residuals.

f/R	F_x	F_y	F_z	τ_x	τ_y	τ_z
f_1	0	0	0	0	0	0
f_2	0	1	0	0	0	0
f_3	0	0	1	0	0	0
f_4	0	0	0	0	0	0
f_5	0	0	0	0	0	0
f_6	0	0	0	0	0	0

matrix is presented in Table 8. It can be seen form Figs. 21–22 that the sensor fault can be effectively detected at 7.7 s in Y-Z direction and the fault signatures would be made immediately.

In order to evaluate the detection performance, the accuracy, the fault detection rate (FDR), the false alarm rate (FAR), and the missed detection rate (MDR) are adopted as the indexes. The accuracy, FDR, FAR, and MDR are defined as follows [44]:

$$Accuracy = \frac{TP + TN}{TP + FP + TN + FN} \tag{45}$$

$$FDR = \frac{TP}{TP + FP} \tag{46}$$

$$FAR = \frac{FN}{TP + FN} \tag{47}$$

$$MDR = \frac{FP}{\text{Total number of faults}} \tag{48}$$

where TP, TN, FP, and FN indicate the number of true positives (fault signal correctly diagnosed as fault), true negatives (normal signal correctly diagnosed as normal), false positives (fault signal incorrectly identified as normal), and false negatives (normal signal incorrectly identified as fault).

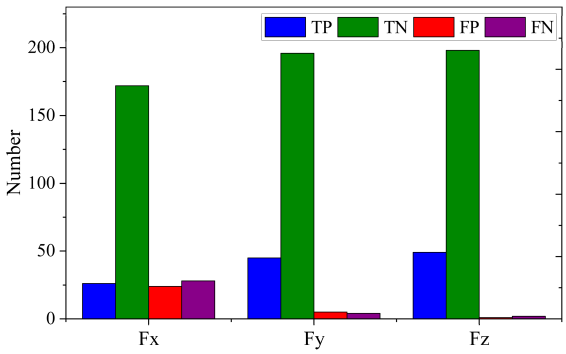

FIGURE 23. The classification results of fault detection.

TABLE 9. The detection performances in X-Y-Z direction.

Performance factors	Fx	Fy	Fz
Accuracy	0.7920	0.9640	0.9880
FDR	0.5200	0.9000	0.9800
FAR	0.5185	0.0816	0.0392
MDR	0.4800	0.1000	0.0200

The experiment of the fault detection was tested for 250 times, with 50 times for sensor faults. The results were divided in two classes; normal and fault. The classification results of fault detection are summarized into bar plots and showed in Fig. 23. Table 9 shows the detection performances in terms of the accuracy, FDR, FAR, and MDR. According to the results showed in Fig. 23. and listed in Table 9, the proposed detection strategy achieved the highest accuracy of 98.80% with the smallest false alarm rate of 3.92% in Z direction. However, the detection performances in X direction

is undesirable due to the high number of FPs and FNs. Note that the sensor failure can be correctly determined once the faulty signal occurs in a certain direction. Hence, the proposed approach can be used to detect the sensor faults in radioactive environments.

VI. CONCLUSION

In this study, a modified disturbance observer (MDO) based scheme is proposed to estimate the unknown external force and detect the sensor faults for a robot manipulator. The stability analysis shows that the proposed method can guarantee the asymptotically convergence of the observer tracking error to be ultimately bounded. The disturbance rejection and tracking performance were greatly improved by using MDO compensation. Simulations and experiments under different practical scenarios are carried out to illustrate the effectiveness of the proposed observer. The results performed on the Kinova Jaco^2 manipulator show that the proposed scheme can evaluate the external disturbance force with the bounded estimated errors and the superiority of the proposed scheme was highlighted by comparing it with the extended state observer (ESO) method. Furthermore, the sensor fault detection was achieved by using the fault signatures from the proposed observer, which can improve the safety and reliability of the robotic system without additional hardware. Hence, the proposed scheme provides an efficient alternative to traditional sensors as well as a redundant solution for the force sensing of robotic systems. Future work will make efforts to achieve sensorless force control of remote robot manipulator in radioactive environment.

APPENDIX

The dynamical parameters of Kinova Jaco^2 manipulator used in simulation are listed as follows:

Parameter	Joint 1	Joint 2	Joint 3	Joint 4	Joint 5	Joint 6
m[kg]	0.7477	0.9962	0.6764	0.4264	0.4264	0.7854
mr_x [kg·m]	0.0016	0.0053	-0.0019	0.0002	0.0052	0.0051
mr_y [kg·m]	0.0017	0.0680	0.0036	-0.0522	0.0026	0.0020
mr_z [kg·m]	0.0032	-0.0036	0.0026	0.0038	0.0221	-0.0008
I_{xx} [kg·m^2]	0.0021	0.0042	0.0030	0.7082	0.8264	0.0046
I_{xy} [kg·m^2]	0.0002	0.0001	0.0002	0.0082	0.0079	0.0002
I_{xz} [kg·m^2]	0.0001	-0.0016	0	0.1130	0.1012	0.0003
I_{yy} [kg·m^2]	0.0008	0.0265	0.0026	0.7412	0.8531	0.0046
I_{yz} [kg·m^2]	-0.0002	0	-0.0032	0.0006	0	0.0003
I_{zz} [kg·m^2]	0.0024	0.0217	0.0034	0.1782	0.1711	0
f_c	1.2405	1.4572	1.680	0.622	0.8364	0.4752
f_v	4.292	5.5232	6.0736	4.0732	4.6326	3.0872

REFERENCES

[1] D. Deng, L. Zhang, M. Dong, R. E. Samuel, A. Ofori-Boadu, and M. Lamssali, "Radioactive waste: A review," *Water Environ. Res.*, vol. 92, no. 10, pp. 1818–1825, 2020.

[2] E. D. Sol, P. Pagala, R. King, and M. Ferre, "External force estimation for telerobotics without force sensor," in *Proc. 1st Iberian Robot. Conf. (ROBOT)*, Cham, Switzerland, 2014, pp. 631–644.

[3] H. Liu, X. Wang, and M. Li, "External force estimation for robotic manipulator base on particle swarm optimization," *Int. J. Adv. Rob. Syst.*, vol. 18, Dec. 2021, Art. no. 17298814211063744.

[4] S. Zhang, S. Wang, F. Jing, and M. Tan, "A sensorless hand guiding scheme based on model identification and control for industrial robot," *IEEE Trans. Ind. Informat.*, vol. 15, no. 9, pp. 5204–5213, Sep. 2019.

[5] S. Haddadin, A. De Luca, and A. Albu-Schäffer, "Robot collisions: A survey on detection, isolation, and identification," *IEEE Trans. Robot.*, vol. 33, no. 6, pp. 1292–1312, Dec. 2017.

[6] B. Yao, Z. Zhou, L. Wang, W. Xu, Q. Liu, and A. Liu, "Sensorless and adaptive admittance control of industrial robot in physical human–robot interaction," *Robot. Comput.-Integr. Manuf.*, vol. 51, pp. 158–168, Jun. 2018.

[7] M. Ragaglia, A. M. Zanchettin, L. Bascetta, and P. Rocco, "Accurate sensorless lead-through programming for lightweight robots in structured environments," *Robot. Comput.-Integr. Manuf.*, vol. 39, pp. 9–21, Jun. 2016.

[8] J. Hu and R. Xiong, "Contact force estimation for robot manipulator using semiparametric model and disturbance Kalman filter," *IEEE Trans. Ind. Electron.*, vol. 65, no. 4, pp. 3365–3375, Apr. 2018.

[9] G. Sebastian, Z. Li, V. Crocher, D. Kremers, Y. Tan, and D. Oetomo, "Interaction force estimation using extended state observers: An application to impedance-based assistive and rehabilitation robotics," *IEEE Robot. Autom. Lett.*, vol. 4, no. 2, pp. 1156–1161, Apr. 2019.

[10] J. M. Daly and D. W. Wang, "Time-delayed output feedback bilateral teleoperation with force estimation for *n*-DOF nonlinear manipulators," *IEEE Trans. Control Syst. Technol.*, vol. 22, no. 1, pp. 299–306, Jan. 2013.

[11] S. K. Kommuri, S. Han, and S. Lee, "External torque estimation using higher order sliding-mode observer for robot manipulators," *IEEE/ASME Trans. Mechatronics*, vol. 27, no. 1, pp. 513–523, Feb. 2022.

[12] W.-H. Chen, D. J. Ballance, P. J. Gawthrop, and J. O'Reilly, "A nonlinear disturbance observer for robotic manipulators," *IEEE Trans. Ind. Electron.*, vol. 47, no. 4, pp. 932–938, Aug. 2000.

[13] W.-H. Chen, J. Yang, L. Guo, and S. Li, "Disturbance-observer-based control and related methods—An overview," *IEEE Trans. Ind. Electron.*, vol. 63, no. 2, pp. 1083–1095, Feb. 2016.

[14] G. Liao, Y. Sheng, and X. Zeng, "Spacecraft hovering around asteroid via disturbance observer based exponential time-varying sliding mode controller," in *Proc. 13th IEEE Int. Conf. Control Autom. (ICCA)*, Ohrid, Macedonia, Jul. 2017, pp. 313–318.

[15] C. Veil, D. Müller, and O. Sawodny, "Nonlinear disturbance observers for robotic continuum manipulators," *Mechatronics*, vol. 78, Oct. 2021, Art. no. 102518.

[16] W. Liang, S. Huang, S. Chen, and K. K. Tan, "Force estimation and failure detection based on disturbance observer for an ear surgical device," *ISA Trans.*, vol. 66, pp. 476–484, Jan. 2017.

[17] A. Mohammadi, M. Tavakoli, H. J. Marquez, and F. Hashemzadeh, "Nonlinear disturbance observer design for robotic manipulators," *Control Eng. Pract.*, vol. 21, no. 3, pp. 253–267, Mar. 2013.

[18] T. N. Truong, A. T. Vo, H.-J. Kang, and T. D. Le, "A neural terminal sliding mode control for tracking control of robotic manipulators in uncertain dynamical environments," in *Proc. Int. Conf. Intell. Comput.*, Cham, Switzerland, Aug. 2021, pp. 207–221.

[19] Z. Chen, F. Huang, W. Chen, J. Zhang, W. Sun, J. Chen, J. Gu, and S. Zhu, "RBFNN-based adaptive sliding mode control design for delayed nonlinear multilateral telerobotic system with cooperative manipulation," *IEEE Trans. Ind. Informat.*, vol. 16, no. 2, pp. 1236–1247, Feb. 2020.

[20] S. Zhen, M. Ma, X. Liu, F. Chen, H. Zhao, and Y.-H. Chen, "Model-based robust control design and experimental validation of SCARA robot system with uncertainty," *J. Vib. Control*, pp. 1–14, Jan. 2022.

[21] Z. Chen, F. Huang, W. Sun, J. Gu, and B. Yao, "RBF-neural-network-based adaptive robust control for nonlinear bilateral teleoperation manipulators with uncertainty and time delay," *IEEE/ASME Trans. Mechatronics*, vol. 25, no. 2, pp. 906–918, Apr. 2020.

[22] T. Yang, N. Sun, Y. Fang, X. Xin, and H. Chen, "New adaptive control methods for n-Link robot manipulators with online gravity compensation: Design and experiments," *IEEE Trans. Ind. Electron.*, vol. 69, no. 1, pp. 539–548, Jan. 2021.
[23] S. Zhang, Y. Dong, Y. Ouyang, Z. Yin, and K. Peng, "Adaptive neural control for robotic manipulators with output constraints and uncertainties," *IEEE Trans. Neural Netw. Learn. Syst.*, vol. 29, no. 11, pp. 5554–5564, Nov. 2018.
[24] Q. Liu, D. Li, S. S. Ge, R. Ji, Z. Ouyang, and K. P. Tee, "Adaptive bias RBF neural network control for a robotic manipulator," *Neurocomputing*, vol. 447, pp. 213–223, Aug. 2021.
[25] Q. Zhou, S. Zhao, H. Li, R. Lu, and C. Wu, "Adaptive neural network tracking control for robotic manipulators with dead zone," *IEEE Trans. Neural Netw. Learn. Syst.*, vol. 30, no. 12, pp. 3611–3620, Dec. 2019.
[26] W. He and Y. Dong, "Adaptive fuzzy neural network control for a constrained robot using impedance learning," *IEEE Trans. Neural Netw. Learn. Syst.*, vol. 29, no. 4, pp. 1174–1186, Feb. 2017.
[27] P. A. Ioannou and J. Sun, *Robust Adaptive Control*. Chelmsford, MA, USA: Courier Corporation, 2012.
[28] A. T. Vo and H.-J. Kang, "Neural integral non-singular fast terminal synchronous sliding mode control for uncertain 3-DOF parallel robotic manipulators," *IEEE Access*, vol. 8, pp. 65383–65394, 2020.
[29] A. T. Vo and H.-J. Kang, "An adaptive neural non-singular fast-terminal sliding-mode control for industrial robotic manipulators," *Appl. Sci.*, vol. 8, no. 12, p. 2562, Dec. 2018.
[30] X. Kong, B. Cai, Y. Liu, H. Zhu, Y. Liu, H. Shao, C. Yang, H. Li, and T. Mo, "Optimal sensor placement methodology of hydraulic control system for fault diagnosis," *Mech. Syst. Signal Process.*, vol. 174, Jul. 2022, Art. no. 109069.
[31] K. O. Omali, M. N. Kabbaj, and M. Benbrahim, "Sensor fault detection and isolation for a robot manipulator based on high-gain observers," in *Proc. 1st Int. Conf. Real Time Intell. Syst.*, Cham, Switzerland, May 2017, pp. 426–435.
[32] F. Piltan, C.-H. Kim, and J.-M. Kim, "Advanced adaptive fault diagnosis and tolerant control for robot manipulators," *Energies*, vol. 12, no. 7, p. 1281, Apr. 2019.
[33] J. Pan, L. Qu, and K. Peng, "Sensor and actuator fault diagnosis for robot joint based on deep CNN," *Entropy*, vol. 23, no. 6, p. 751, Jun. 2021.
[34] L. Yao, L. Zuo, and B. Hong, "Fault diagnosis and fault-tolerant control of networked manipulator system with actuator fault," *Int. J. Innov. Comput., Inf. Control*, vol. 16, no. 6, pp. 2021–2034, Dec. 2020.
[35] B. Siciliano, L. Sciavicco, L. Villani, and G. Oriolo, *Advanced Textbooks in Control and Signal Processing*, 2nd ed. London, U.K.: Springer, 2009.
[36] Z. A. Khan, V. Chacko, and H. Nazir, "A review of friction models in interacting joints for durability design," *Friction*, vol. 5, no. 1, pp. 1–22, Mar. 2017.
[37] K. Ohnishi, M. Shibata, and T. Murakami, "Motion control for advanced mechatronics," *IEEE/ASME Trans. Mechatron.*, vol. 1, no. 1, pp. 56–67, Mar. 1996.
[38] A. Mohammadi, H. J. Marquez, and M. Tavakoli, "Nonlinear disturbance observers: Design and applications to Euler–Lagrange systems," *IEEE Control Syst. Mag.*, vol. 37, no. 4, pp. 50–72, Jul. 2017.
[39] H. J. Marquez, *Nonlinear Control Systems: Analysis and Design*, vol. 161. Hoboken, NJ, USA: Wiley, 2003.
[40] G. Golluccio, G. Gillini, A. Marino, and G. Antonelli, "Robot dynamics identification: A reproducible comparison with experiments on the Kinova Jaco," *IEEE Robot. Autom. Mag.*, vol. 28, no. 3, pp. 128–140, Sep. 2021.
[41] J. Jin and N. Gans, "Parameter identification for industrial robots with a fast and robust trajectory design approach," *Robot. Comput.-Integr. Manuf.*, vol. 31, pp. 21–29, Feb. 2015.
[42] Z. Gao, "Scaling and bandwidth-parameterization based controller tuning," in *Proc. Amer. Control Conf.*, Denver, CO, USA, Jun. 2006, pp. 4989–4996.
[43] Y. R. Stürz, L. M. Affolter, and R. S. Smith, "Parameter identification of the KUKA LBR iiwa robot including constraints on physical feasibility," *IFAC-PapersOnLine*, vol. 50, no. 1, pp. 6863–6868, Jul. 2017.
[44] M. Alauddin, F. Khan, S. Imtiaz, and S. Ahmed, "A variable mosquito flying optimization-based hybrid artificial neural network model for the alarm tuning of process fault detection systems," *Process Saf. Prog.*, vol. 39, no. S1, Mar. 2020, Art. no. e12122.

HUAIMIN LIU received the B.S. and M.S. degrees in mechanical engineering from the University of South China, Hengyang, China, in 2013 and 2016, respectively, where he is currently pursuing the Ph.D. degree with the College of Resource Environmental and Safety Engineering. His research interests include robot force control and teleoperation.

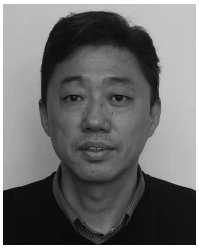

XIANGJIANG WANG received the B.S. degree in mechanical engineering from the Harbin Institute of Technology, Harbin, China, in 1994, and the Ph.D. degree in mechanical engineering from Southeast University, Nanjing, China, in 2008. From 2012 to 2013, he was a Visiting Professor at the University of Wollongong, Australia. He is currently a Professor with the Department of Mechanical Engineering, University of South China, Hengyang, China. His research interests include nonlinear control, nuclear robotics, and teleoperation control.

LIUYANG CHEN received the B.S. degree in mechanical engineering from the University of South China, Hengyang, China, in 2020, where she is currently pursuing the master's degree with the Department of Mechanical Engineering. Her research interests include robot force control and nuclear robotics.